A multidisciplinary approach to quantify the permeability of the Whakaari/White Island volcanic hydrothermal system (Taupo Volcanic Zone, New Zealand)

Michael J. Heap[1], Ben M. Kennedy[2], Jamie I. Farquharson[1], James Ashworth[3], Klaus Mayer[4], Mark Letham-Brake[5], Thierry Reuschlé[1], H. Albert Gilg[6], Bettina Scheu[4], Yan Lavallée[3], Paul Siratovich[2], Jim Cole[2], Arthur D. Jolly[7], Patrick Baud[1], Donald B. Dingwell[4]

[1]*Géophysique Expérimentale, Institut de Physique de Globe de Strasbourg (UMR 7516 CNRS, Université de Strasbourg/EOST), 5 rue René Descartes, 67084 Strasbourg cedex, France.*

[2]*Geological Sciences, University of Canterbury, Private Bag 4800, 8140 Christchurch, New Zealand*

[3]*Earth, Ocean and Ecological Sciences, University of Liverpool, Liverpool L69 3GP, United Kingdom.*

[4]*Earth & Environmental Sciences, Ludwig Maximilians Universität, Theresienstr. 41/III, 80333 Munich, Germany.*

[5]*Kakapo Disaster Resilience, 2/48 Brockworth Place, Riccarton 8011, Christchurch, New Zealand.*

[6]*Lehrstuhl für Ingenieurgeologie, Technische Universität München, Arcisstr. 21, 80333 Munich, Germany.*

[7]*GNS Science, 1 Fairway Avenue Avalon, 5040, New Zealand.*

Keywords: Alteration; Fracture; Porosity; Permeability; Lava; Tuff; Pore pressure

Corresponding author: M.J Heap (heap@unistra.fr)

Highlights

- Whakaari chiefly comprises lavas, lava breccias, ash tuffs, and tephra.
- Porosity varies from ~0.01 to ~0.7 and permeability from ~10^{-19} to ~10^{-11} m^2.
- The spatial distribution of rock types in crater walls and crater-fill deposits identifies vertical and horizontal barriers to and pathways for fluid transport.
- Pore- and fracture-filling precipitation and cementation can locally reduce porosity and permeability and therefore augment pore pressure.
- Our data will assist the modelling of deformation, seismicity, and explosive behaviour at active hydrothermal systems worldwide.

Abstract

Our multidisciplinary study aims to better understand the permeability of active volcanic hydrothermal systems, a vital prerequisite for modelling and understanding their behaviour and evolution. Whakaari/White Island volcano (an active stratovolcano at the north-eastern end of the Taupo Volcanic Zone of New Zealand) hosts a highly reactive hydrothermal system and represents an ideal natural laboratory to undertake such a study. We first gained an appreciation of the different lithologies at Whakaari and (where possible) their lateral and vertical extent through reconnaissance by land, sea, and air. The main crater, filled with tephra deposits, is shielded by a volcanic amphitheatre comprising interbedded lavas, lava breccias, and tuffs. We deployed field techniques to measure the permeability and density/porosity of (1) more than 100 hand-sized sample blocks and (2) layered unlithified deposits in eight purpose-dug trenches. Our field measurements were then groundtruthed using traditional laboratory techniques on almost 150 samples. Our measurements highlight that the porosity of the materials at Whakaari varies from ~0.01 to ~0.7 and permeability varies by eight orders of magnitude (from $\sim10^{-19}$ to $\sim10^{-11}$ m^2). The wide range in physical and hydraulic properties is the result of the numerous lithologies and their varied microstructures and alteration intensities, as exposed by a combination of macroscopic and microscopic (scanning electron microscopy) observations, quantitative mineralogical studies (X-ray powder diffraction), and mercury porosimetry. An understanding of the spatial distribution of lithology and alteration style/intensity is therefore important to decipher fluid flow within the Whakaari volcanic hydrothermal system. We align our field observations and porosity/permeability measurements to construct a schematic cross section of Whakaari that highlights the salient findings of our study. Taken together, the alteration typical of a volcanic hydrothermal system can result in increases (due to alteration-induced dissolution and fracturing) and decreases (due to hydrothermal precipitation) to permeability. Importantly, a decrease in

permeability—be it due to fracture sealing in the lava, pore-filling alunite precipitation in the tuffs, near-vent cementation by sulphur, and/or well-sorted layers of fine ash—can result in pore pressure augmentation. An increase in pore pressure could result in ground deformation, seismicity, jeopardise the stability of the volcanic slopes, and/or drive the wide variety of eruptions observed at Whakaari. Our systematic study offers the most complete porosity-permeability dataset for a volcanic hydrothermal system to date. These new data will inform and support modelling, unrest monitoring, and eruption characterisation at Whakaari and other hydrothermally modified volcanic systems worldwide.

1. Introduction

The permeability of the materials within a volcanic hydrothermal system controls the ease at which exsolved magmatic volatiles can escape the magma-filled conduit (*Eichelberger et al.*, 1987; *Jaupart*, 1998; *Collinson and Neuberg*, 2012), as well as the ingress, circulation, and interaction of meteoric and/or marine (in the case of volcanic islands, coastal, or submarine volcanoes) water and hydrothermal fluids (*Bibby et al.*, 1995; *Edmonds et al.*, 2003; *Rowland and Sibson*, 2004; *Hurwitz et al.*, 2007). The permeability of a volcanic hydrothermal system therefore exerts a first-order control on the magnitude and distribution of pore pressure (*Hurwitz et al.*, 2007; *Todesco et al.*, 2010; *Fournier and Chardot*, 2012). The build-up of pore pressure within a volcanic hydrothermal system can lead to catastrophic flank collapse (*Day*, 1996; *Voight and Elsworth*, 1997; *Reid et al., 2001; Reid*, 2004; *Moon et al.*, 2009; *Procter et al.*, 2014), seismicity (*Nishi et al.*, 1996; *Sherburn et al.*, 1998; *Bean et al.*, 2014; *Chardot et al.*, 2015), and/or drive a wide variety of eruptions, from phreatic (*Barberi et al.*, 1992; *Kaneshima et al.*, 1996; *Christenson et al.*, 2010; *Mayer et al.*, 2015; *Montanaro et al.*, 2016; *Mayer et al.*, 2016a; 2016b) and phreatomagmatic (*Bertagnini et al.*, 1991; *Houghton and Nairn*, 1991) explosions to larger, more sustained eruptions (*Houghton and Nairn*, 1991; *Christenson*, 2000; *Deino et al.*, 2004). Detailed knowledge of the permeability of the materials found within hydrothermal systems will therefore provide a deeper understanding of their behaviour and evolution (*Hurwitz et al.*, 2007; *Collombet*, 2009; *Todesco et al.*, 2010; *Christenson et al.*, 2010; *Fournier and Chardot*, 2012; *Collinson and Neuberg*, 2012).

While laboratory studies have exposed porosity-permeability relationships for a variety of volcanic rocks (*Klug and Cashman*, 1996; *Saar and Manga*, 1999; *Rust and Cashman*, 2004; *Mueller et al.*, 2005; *Wright et al.*, 2009; *Farquharson et al.*, 2015; *Kushnir et al.*, 2016; *Wadsworth et al.*, 2016; *Heap and Kennedy,* 2016), studies that provide values of permeability for the highly altered lithologies that typically comprise

hydrothermal systems are scarce (*Siratovich et al*., 2014; *Mayer et al.,* 2016a; 2016b), largely due to their microstructural complexity and variability. To emphasise, hydrothermal alteration can be the result of dissolution, mineral precipitation, and secondary mineralisation (*Browne*, 1978) and can therefore result in increases or decreases in porosity, a physical property known to exert a first-order control on permeability (e.g., *Bourbié and Zinszner*, 1985). For example, the hydrothermal alteration of volcanic rocks can replace the existing minerals with weak minerals such as clays (e.g., kaolinite, illite, and smectite; *Steiner*, 1968; *Browne*, 1978; *Inoue*, 1995) and sulphates (e.g., alunite and jarosite; *Johnston*, 1977; *Ece et al*., 2008), leading to material weakening (*del Potro and Hürlimann*, 2009; *Pola et al*., 2012; 2014; *Frolova et al*., 2014; *Wyering et al.*, 2014; 2015; *Heap et al*., 2015a), fracturing/disintegration, and therefore an increase in permeability. On the other hand, hydrothermal alteration can infill pores and fractures (both micro- and macrofractures) with precipitated minerals (*Edmonds et al*., 2003; *Wyering et al.*, 2014; *Heap et al*., 2015a; *Ball et al*., 2015) leading to reductions in permeability (e.g., *Griffiths et al*., 2016). The type and intensity of hydrothermal alteration will not only depend on the rock type, but also on the temperature (*Wyering et al.*, 2014; *Frolova et al*., 2014) and composition (including pH) of the circulating fluids, and the effective fluid-rock ratio (*Browne*, 1978; *Reed*, 1997), factors that can vary tremendously in both space and time. The consequence of this variability is that the rocks within a volcanic hydrothermal system will suffer a broad array of chemical alteration that will modify their physical properties, such as porosity and permeability, in different ways and to different degrees.

And so it is that, especially for volcanic hydrothermal systems, an understanding of the permeability—and therefore behaviour—must rely on a detailed comprehension of the variability in porosity and permeability of the accumulated materials, and information as to their spatial distribution. Whakaari volcano (an active stratovolcano located at the north-eastern end of the Taupo Volcanic Zone of New Zealand) hosts an

127 open, highly reactive hydrothermal system (hot springs and mud pools, fumaroles, acid
128 streams and lakes) (*Giggenbach et al.,* 2003 and references therein) and represents an
129 ideal natural laboratory to undertake such a study. We present herein a
130 multidisciplinary study designed to better understand the permeability of an active
131 volcanic hydrothermal system. The primary goal of this contribution is to produce a
132 very large dataset to inform future modelling efforts. The permeability of the materials
133 within active volcanic hydrothermal systems is, for example, required to understand
134 and accurately model the outgassing of magmatic volatiles from the magma-filled
135 conduit (*Collombet*, 2009; *Collinson and Neuberg*, 2012), subsurface hydrothermal
136 activity and therefore volcanic unrest (*Hurwitz et al*., 2007; *Peltier et al.*, 2009; *Todesco*
137 *et al*., 2010; *Christenson et al*., 2010 *Fournier and Chardot*, 2012; *Christenson et al*., 2016),
138 gas monitoring (*Bloomberg et al*., 2014; *Peiffer et al*., 2014), and volcano seismicity (*Leet*,
139 1988; *Nishi et al*., 1996; *Sherburn et al*., 1998; *Bean et al*., 2014; *Chardot et al*., 2015).
140

141 **2. Whakaari (White Island volcano)**

142 Whakaari is an active andesitic-dacitic stratovolcano located 48 km north of
143 New Zealand's North Island, at the north-eastern end of the Taupo Volcanic Zone (Figure
144 1). The island, the tip of a much larger submarine structure, summits at 321 m above sea
145 level and measures 2.4 km east–west by 2 km north–south (*Clark and Cole*, 1986;
146 *Houghton and Nairn*, 1991 and references therein). Whakaari's subaerial structure
147 consists of two cones: the extinct and partially eroded Ngatoro Cone and the active,
148 amphitheatre-shaped Central Cone (Figure 1). Both are constructed from lavas, tuffs,
149 agglomerates, tephra, dykes, and breccias (*Cole et al.*, 2000 and references therein).
150 Geomorphic evidence suggests that 0.21 km^3 of material was prehistorically removed
151 from the Central Cone due to major flank failures involving weak hydrothermally
152 altered rock (*Moon et al*., 2009).

153 Whakaari hosts an open, highly reactive hydrothermal system that has existed
154 for approximately 10, 000 years (*Giggenbach et al.,* 2003 and references therein). The
155 mélange of marine/meteoric water and hot magmatic fluids generate acid brines
156 (*Giggenbach et al.,* 2003 and references therein; *Christenson et al*., 2016) that rise to the
157 surface forming hot springs, mud pools, fumaroles, and acid streams and lakes. The pH
158 of the acid streams can be as low as ~2 (*Hedenquist et al*., 1993; *Donachie et al*., 2002).
159 Crater lake, a large lake of boiling acidic waters in the western subcrater, which appears
160 to vary in volume due to meteorological conditions and fluctuating levels of
161 hydrothermal activity (*Christenson et al*., 2016), is the focus of present day volcanic
162 activity and outgassing (e.g., *Werner et al*., 2008; *Bloomberg et al*., 2014), although more
163 diffuse outgassing through the crater floor and outgassing through fumaroles that line
164 the crater rim is also observed (*Bloomberg et al*., 2014).
165 Volcanic eruptions at Whakaari are generally phreatic or phreatomagmatic in
166 style (although Strombolian activity occurred from the late seventies to the mid-
167 eighties; *Houghton and Nairn*, 1991), and form discrete craters within the main crater-
168 fill deposits of the Central Cone (*Houghton and Nairn*, 1991; *Cole et al.*, 2000). Indeed, a
169 minimum of 28 phreatic or phreatomagmatic eruptions has occurred since 1826 (*Mayer*
170 *et al*., 2015). Prehistoric eruptions at Whakaari, recorded in the stratigraphy of crater
171 walls of the Central Cone, were characterised by the extrusion of lava (*Cole et al.*, 2000).
172 Eruptions at Whakaari are frequent to this day, the most recent occurring on April 27
173 2016.
174 Geophysical surveys on main crater floor highlight ground deformation episodes
175 within the recently formed eruption centres and fumarole fields, interpreted as an
176 increase in pore pressure due to the migration of hydrothermal fluids and/or shallow
177 magma injection (e.g., *Peltier et al.*, 2009; *Fournier and Chardot*, 2012) and/or lake level
178 variations (*Christenson et al*., 2016). The circulation of hydrothermal fluids within these
179 zones has been blamed for swarms of low-amplitude, high-frequency earthquakes and

180 volcanic tremors (*Nishi et al.*, 1996; *Sherburn et al.*, 1998; *Chardot et al.*, 2015). Although
181 the permeability of the main crater floor has been inferred from thermal infrared
182 mapping (*Mongillo and Wood*, 1995) and gas and heat flux mapping (*Bloomberg et al.*,
183 2014), a systematic study that provides direct measurements of permeability, to our
184 knowledge, is not currently available.
185
186 **3. Reconnaissance of Whakaari by land, sea, and air**
187 In order to assess the lateral and (where possible) vertical extent of the main
188 lithologies at Whakaari, and therefore select the most appropriate rocks for our study,
189 we lean on decades of reconnaissance missions of the island by land, sea, and air
190 (summarised in Figure 2). We also consulted historical records.
191 The modern-day crater walls chiefly comprise interbedded coherent (albeit
192 fractured) and brecciated lavas dipping away from the centre of the island. These
193 sequences of interbedded lava and lava breccia deposits can reach >100 m in thickness
194 (Figure 2, picture 1). Significant debris from the lava breccia deposit from the north-
195 eastern wall of the volcanic amphitheatre (Figure 2, picture 7) can be seen at the base of
196 the slope (Figure 3c).
197 Interbedded tuffs with a dominantly ash-sized particle size (hereafter called ash
198 tuffs) and coarser lithified pyroclastic deposits (lapilli tuffs) are exposed in perched
199 subcraters within the main crater walls (Figure 2; pictures 9, 10, and 11) and sequences
200 can reach >10 m in thickness. Bedded sequences of ash and lapilli tuffs, interbedded
201 with the lavas and lava breccias, dip away from the volcano, as seen in the eastern and
202 western sea cliffs of the volcano (Figure 2; pictures 10, 12, 15, 16). Coarse lithified
203 pyroclastic deposits also fill pre-existing valleys and are exposed in the cliffs on the
204 outer flanks of the volcano.

All of the interbedded deposits forming the crater walls are blanketed by layers of recent tephra deposits comprised of mostly well sorted ash and lapilli airfall (Figure 2; Figures 3a-b).

The crater rim is lined with active fumaroles, boiling mud pools, and acid streams (Figure 2; pictures 2, 4, and 6; Figures 3d-f). The crater-fill deposits found in these areas have been locally cemented by hydrothermal activity (frequently by sulphur or sulphates), forming lithified crusts (Figure 2; pictures 2, 4, and 6; Figures 3d-f). Fumaroles are encrusted by sulphur and sulphur flows are seen—albeit rarely—to extend from fumaroles containing subsurface pools of liquid sulphur (Figure 3f).

The main crater is filled with unlithified ash and lapilli deposits that are at least several metres in thickness and consist of numerous thin beds (from several mm to several cm in thickness) that can be easily distinguished based on their differences in colour (Figure 3g). The crater floor is strewn with conspicuous rocky hummocks, the debris from the collapse of the crater wall in September 1914 (*Houghton and Nairn*, 1991) (Figure 2, picture 3). Some areas close to the current crater lake—such as the area near Donald Duck and Noisy Nellie craters (Figures 3h-i)—are blanketed by a well-sorted layer of fine ash ~100 mm in thickness. Eruptions as recent as 2016 have carpeted the crater floor deposits with blocks (Figure 2; Figures 3g-i) and poorly sorted surge deposits that are rapidly reworked into fluvial deposits draining away from the main crater towards the sea (Figure 2; pictures 2 and 3).

The mapped surface exposure of deposits is further informed by historic accounts, photos, published articles, and volcano monitoring (GeoNet) reports outlining geomorphological changes to the crater. Eruptions have generated ~15 overlapping explosion craters and subsidence pits (up to 200 m deep) in the northern end of the main crater (*Houghton and Nairn*, 1989) that have been rapidly filled with eruption and erosional debris. Lava is occasionally seen within these craters either as a small dome (*Chardot et al.*, 2014) or as a distinct glow (*Houghton and Nairn*, 1989). Surges and

232 ballistic debris generate tuff cones (*Jolly et al.*, 2016) in and around the modern crater
233 lake. Debris avalanches, landslides, and rockfalls deposit material on the crater floor and
234 create curvilinear collapse scars in the crater walls (e.g., *Moon et al.*, 2009). These
235 catastrophic events are further modified by erosion and shifting drainages, as
236 hydrothermal waters make their way south-east towards the ocean via surface streams.
237 Our reconnaissance has highlighted the extreme complexity and variability of
238 the lithologies that form or are found within the crater at Whakaari. To best capture this
239 variability we chose to (1) collect in excess of a hundred rock blocks for field and
240 laboratory porosity-permeability testing and, (2) perform field porosity-permeability
241 measurements on numerous vertical transects through the unlithified crater floor
242 deposits. We also collected two unlithified crater floor samples for porosity-
243 permeability measurement in the laboratory.
244
245 **4. Materials and methods for the lithified materials**
246
247 *4.1 Description of the lithified materials*
248 We collected 124 blocks representative of the deposits that form or are found
249 within the crater at Whakaari: 115 hand-sized sample blocks (approximately 100 × 100
250 × 100 mm, although their shape varied; see Figures A1-A5) and nine larger blocks
251 (approximately 300 × 300 × 300 mm). The hand-sized sample blocks were collected
252 from three sites located within the crater: the accessible scree at (1) the foot of the
253 eastern wall of the volcanic amphitheatre near Shark Bay, (2) Wilson's Bay and, (3) the
254 foot of the northern wall of the volcanic amphitheatre near Noisy Nellie crater (sampling
255 sites are shown on Figure 1). These sites were selected due to their accessibility and
256 because they contained blocks representative of the range of materials observed during
257 our reconnaissance (Figures 2 and 3). The locations on the volcanic slopes that fed these
258 scree deposits could be readily identified by fresh rockfall scars at each collection site.

259 The blocks consisted of variably altered ash tuffs (i.e., tuffs with an ash-sized particle
260 size), lavas, and lava breccias (Figures A1-A5). The hand-sized sample blocks were
261 collected for measurements of field density/porosity and permeability and, after coring
262 20 mm-diameter cylindrical samples from the blocks, measurements of porosity and
263 permeability in the laboratory. The goal of these measurements was to provide a large
264 porosity-permeability dataset; more detailed analyses (scanning electron microscopy
265 (SEM), X-ray powder diffraction (XRPD), and mercury porosimetry) were performed on
266 the nine larger blocks collected. These nine blocks, five of which were used in the recent
267 studies of *Heap et al*. (2015a) and *Mayer et al*. (2015), were selected to best represent
268 the variability seen at Whakaari (Figures 2 and 3). We collected one block of lava, one
269 block of lava breccia, four blocks of ash tuffs, one block of sulphur flow, one block of
270 sulphur crust, and one block of jarosite crust. Thin sections (double-polished) of each of
271 these rocks were made for SEM analysis and XRPD analysis was performed at the
272 Technische Universität München (TUM, Germany) on powdered material of each of the
273 blocks. For the XRPD analysis, powdered samples were mixed with an internal standard
274 (10% ZnO) and ground for 8 min with 10 ml of isopropyl alcohol in a McCrone
275 Micronising Mill using agate cylinder elements. The XRPD analyses were performed on
276 powder mounts using a PW 1800 X-ray diffractometer (CuKα, graphite monochromator,
277 10 mm automatic divergence slit, step-scan 0.02° 2θ increments per second, counting
278 time 1 s per increment, 40 mA, 40 kV). The crystalline and amorphous phases in the
279 whole rock powders were quantified using the Rietveld program BGMN (*Bergmann et*
280 *al.*, 1998). To confirm the presence of any identified clay minerals, we also separated <2
281 μm fractions by gravitational settling and prepared oriented mounts that were X-rayed
282 in an air-dried and ethylene glycolated state.

283 The porphyritic andesite lava (WI20) contains a groundmass of hydrated
284 amorphous glass embedded with phenocrysts and microlites of feldspar and pyroxene.
285 The lava is locally fractured and oxidised (Figure 4a). The block was collected at the foot

286 of the eastern wall of the volcanic amphitheatre near Shark Bay (Figures 1, 2, and 3a-b)
287 and likely therefore originates from one of the competent lava units of the currently
288 active Central Cone (*Cole et al*., 2000). Scanning electron microscopy (SEM) has revealed
289 the presence of pervasive microcracking and minor precipitation of alteration minerals
290 (jarosite and gypsum) into some of the pores (Figure 4a). The pores are typically a
291 couple of hundred microns in diameter, although some phenocrysts have microporous
292 rims (Figure 4a). XRPD analysis highlights the main mineralogical components to be
293 plagioclase (37 wt.%), cristobalite (14 wt.%), amorphous silica (14 wt.%), K-feldspar
294 (14 wt.%), and pyroxene (10 wt.%) (Table 1).

295 The altered lava breccia collected (WI30) was taken from the deposit shown in
296 Figure 3c (located within the debris from the partial collapse of the north-eastern wall
297 of the volcanic amphitheatre (Figure 2, picture 7)). Although some of the clasts within
298 the deposit were on the order of 1 m (Figure 3c), we collected material that contained a
299 maximum clast size of ~10 mm in diameter due to the small size of our laboratory
300 samples (20 mm in diameter). The groundmass of the lava breccia is brown-red in
301 colour (due to oxidation) and hosts numerous angular lava fragments (Figure 4l). SEM
302 analysis shows microcracks, zones of microlitic groundmass, and pores up to 500
303 microns in diameter (Figure 4l). The sample consists of amorphous silica (74 wt.%),
304 kaolinite (10 wt.%), and plagioclase (8 wt.%) (Table 1).

305 The four ash tuff deposits are composed of partially cemented ash particles,
306 typically altered crystal fragments or completely opalised shards of glass (now
307 composed dominantly of hydrated amorphous silica). The ash tuff blocks collected were
308 selected based on observable differences in colour (alteration type), macroscopic
309 textures (presence/absence of bedding or laminations), particle size, and degree of
310 cementation. They were all collected in the accessible scree at the foot of the eastern
311 wall of the volcanic amphitheatre near Shark Bay (Figures 1, 2, and 3a-b). The ash tuffs
312 can be subdivided into two subgroups: fine-grained white deposits containing pore-

313 filling alunite (WI21 and WI24) and coarser-grained, bedded deposits that do not
314 contain alunite (WI22 and WI23). Of the deposits containing alunite (WI21 and WI24;
315 Table 1), WI21 contains a lower porosity grey zone (Figure 4b) and a higher porosity
316 white zone that contains gas elutriation pipes (Figure 4c). All gas elutriation pipes were
317 orientated perpendicular to bedding (Figure 4c). WI21 and WI24 contain average
318 particle diameters of ~0.1 and ~0.2 mm, respectively, and an average pore diameter of
319 ~100-200 microns (Figures 4b-c and 4f). Pore-filling alunite (Figure 5) likely
320 precipitated following complete devitrification and opal replacement (*Heap et al.*,
321 2015a). Of the bedded deposits (WI22 and WI23), the grey-coloured WI22 contains an
322 average particle diameter of ~0.3 mm and 10 mm-thick alternating bands of high- and
323 low-porosity (Figure 4d). WI23 contains alternating 3-10 mm-thick alternating brown-
324 red and grey coloured bands (Figure 4e). The average particle diameter varies between
325 the different bands in WI23, from ~0.3-0.4 mm in one band to ~0.1 mm in another
326 (Figure 4e). Both WI22 and WI23 contain and an average pore diameter of ~100-200
327 microns (Figures 4d and 4e). The mineral composition of all four ash tuffs is given in
328 Table 1. While these tuffs can be described as *completely* altered (they contain none of
329 their original mineral phases; classified following British Standard practice *BS5930*,
330 1999), the presence of alunite attests to the mobility of aluminium and therefore
331 precludes the use of chemical alteration indices such as the Chemical Index of Alteration
332 (CIA), the Chemical Index of Weathering (CIW), and the Plagioclase Index of Alteration
333 (PIA) (see *Pola et al.*, 2012).

334 The remaining three lithologies represent those that have been lithified as a
335 result of their proximity to acid streams and fumaroles (Figures 2 and 3d-f). They are:
336 sulphur flow, sulphur crust, and jarosite crust. All of these blocks were collected at the
337 south-western margin of the volcanic amphitheatre (Figures 2 and 3d-f). The sulphur
338 flow is a very dense rock that forms a layer ~100 mm in thickness located next to an
339 active sulphur fumarole (Figure 3f). SEM (Figure 4k) and XRPD (Table 1) analyses

shows that the rock comprises few angular ash fragments that are efficiently cemented together by sulphur. Pores are difficult to distinguish, although microcracks are present (Figure 4k). The sulphur crust block was collected adjacent to the sulphur flow (Figure 3f). The sulphur crust is very heterogeneous and contains ash and lapilli fragments (of devitrified glass, pyroxene, and plagioclase; Table 1) cemented by sulphur (Figure 4h). The sulphur gives the rock its light-green/chartreuse colour. Pores in the sulphur crust are typically ~400-500 microns in diameter (Figure 4h). The jarosite crust is similarly heterogeneous, containing ash and lapilli fragments (of devitrified glass, pyroxene, plagioclase, and cristobalite; Table 1) cemented by jarosite (Figure 4g). Pores in the jarosite crust are typically a couple of hundreds microns in diameter (Figure 4h), but can reach 1 mm in diameter. The mineral composition of all three deposits is given in Table 1.

4.2 Methods for the lithified materials

4.2.1 Field methods

Following several hours of drying in the sun, the permeability of the 115 blocks was estimated using a portable air permeameter (Vindum Engineering TinyPerm II). The TinyPerm unit estimates the permeability by evacuating the air from the rock at the nozzle-rock interface (inner diameter of the nozzle = 10 mm) and monitoring the response function of the transient vacuum. The TinyPerm is a useful field tool that quickly provides an estimate of the permeability of a porous rock, and has been recently used in studies on volcanic materials (*Farquharson et al.*, 2015; *Schaefer et al.*, 2015; *Kendrick et al.*, 2016). Although the TinyPerm II unit cannot provide values of permeability below 6.92×10^{-16} m^2, it has been shown to be reasonably reliable in the range 10^{-12} to 10^{-15} m^2 (*Farquharson et al.*, 2015). However, we note that some of our bedded ash tuff blocks were rectangular prisms (~50-60 mm in thickness); as a result,

permeability estimates on these blocks were likely overestimated by the TinyPerm due to the volume of rock required for near-surface measurements of permeability (*Selvadurai and Selvadurai*, 2010). Estimates of permeability using the TinyPerm unit are not necessarily reliable for small (<<100 mm) samples. Some of the blocks collected appeared to have low-permeability skins; when present, we tried to remove the skin with a file prior to measurement. The permeability of each block was estimated using the mean of 3-4 TinyPerm values measured at different locations on the surface of the block.

The bulk density of each of the 115 hand-sized sample blocks was estimated using the Archimedean weighing technique similar to that employed by *Kueppers et al*. (2005) and *Farquharson et al*. (2015). The dry weight *Wd* of each block was first measured using a balance (precision 0.1 g). The apparent immersed weight *Wi* was then measured by lowering each block into a water-filled bag suspended underneath a balance mounted on a tripod. The immersed weight was taken quickly to avoid water imbibition. The dry bulk density ρ_b of each block could then be determined using the following relation (assuming that the density of water = 1000 kg/m^3):

$$\rho_b = \frac{Wd}{Wd - Wi} \quad (1)$$

Four of the samples (WI-F-16, 46, 59, and 77; Table A2) floated and we could not therefore determine their dry bulk density.

These dry bulk density values were converted to values of total porosity by measuring the solid density of each block. Once back in the laboratory, the blocks were cored to provide 20 mm-diameter cylindrical samples for laboratory measurements of porosity and permeability (see next section). The remainder of each block was powdered using a pestle and mortar. The solid density ρ_s (the density of each powder)

was then measured using a helium pycnometer (Micromeritics AccuPyc II 1340). Total porosity was then determined for each block using the following relation:

$$\phi_t = 1 - \left(\frac{\rho_b}{\rho_s}\right) \quad (2)$$

The total porosity of the four samples that floated (WI-F-16, 46, 59, and 77; Table A2) was estimated by assuming a bulk dry density of 1000 kg/m^3.

4.2.1 Laboratory methods

While field methods provide quick estimates for values of permeability and dry bulk density, such methods should always be groundtruthed by well-constrained measurements in the laboratory. Cylindrical samples (20 mm in diameter) were cored from the 115 hand-sized sample blocks and were precision ground so that their end faces were flat and parallel (Figures A6-12). Samples were cored perpendicular to bedding, where present. The length of each core, which varied from ~22 to ~40 mm, was a function of the size and shape of the block. The length to width ratio of our samples was therefore greater than one in each case (length to width ratios lower than one are not recommended for laboratory permeability measurements). The samples were washed using water and then dried at 40 °C in a vacuum oven for at least two days. The connected porosity of each core sample was measured using a helium pycnometer (Micromeritics AccuPyc II 1340). The samples were then jacketed (in a rubber jacket) and their permeability measured using a benchtop steady-state permeameter (see *Farquharson et al*., 2016; *Heap and Kennedy*, 2016) under a confining pressure of 1 MPa and at ambient laboratory temperature. A confining pressure during routine measurements of permeability is required to prevent gas travelling between the sample and the jacket. Samples were first left for one hour at a confining pressure of 1 MPa to ensure microstructural equilibrium. Flow rate measurements were taken (using either a

418 low- or high-flow gas flowmeter, depending on the permeability of the sample) under
419 several pressure gradients (typically from 0.05 to 0.2 MPa, equating to flow rates
420 between 0.2 and 400 ml/min) to determine the permeability using Darcy's law and to
421 assess the need for the Forchheimer and/or the Klinkenberg corrections, which were
422 applied on a case-by-case basis. The Klinkenberg correction corrects for gas slippage
423 (*Klinkenberg*, 1941), and was typically applied to low-porosity, low-permeability
424 samples with a high microcrack density. The Forchheimer correction corrects for flow
425 inertia and was typically employed for high-permeability samples that had to be
426 measured using high flow rates.

427 Cylindrical samples (20 mm in diameter) were also taken from the nine larger
428 blocks (WI20-26 and WI29-30) and precision ground to a nominal length of 40 mm
429 (Figures 4 and A6-12). Samples of the lava (WI20) were cored so as to contain none or
430 one macroscopic (i.e., sample size) fracture along their axis (Figure 4a). Samples of ash
431 tuff WI21 were prepared to contain (1) no gas elutriation pipes (Figure 4b), (2) gas
432 elutriation pipes parallel to the sample axis (Figure 4c) and, (3) gas elutriation pipes
433 perpendicular to the sample axis (Figure 4c). Samples WI22 and WI23 were cored
434 perpendicular to the bedding direction (Figures 4d and 4e). The porosity and
435 permeability of these samples were measured using the same techniques described
436 above (data are available in Tables A4-A6). Further, to understand the influence of
437 confining pressure (i.e., depth) on permeability, we performed experiments in which we
438 sequentially measured the permeability of a sample of lava (WI20) and ash tuff (WI21)
439 under confining pressures of 1, 2, 5, 10, 15, 20, 25, and 30 MPa (data available in Table
440 A7).

441 To explore their microstructure further, mercury injection tests were performed
442 on pieces (2-5 g) of lava (WI20) and ash tuff (WI21-24) using the Micromeritics
443 Autopore IV 9500 at the University of Aberdeen (Scotland). The evacuation pressure
444 and evacuation time were 50 μmHg and 5 minutes, respectively, and the mercury filling

445 pressure and equilibration time were 0.52 pounds per square inch absolute (psia) and
446 10 seconds, respectively. The pressure range was 0.1 to 60000 psia (i.e., up to a pressure
447 of about 400 MPa). Mercury injection data permit the calculation of the pore throat size
448 distribution within a particular sample.
449
450 **5. Materials and methods for the unlithified materials**
451
452 *5.1 Field materials and methods for the unlithified materials*
453 Eight localities within the recent, unlithified deposits of the crater floor at
454 Whakaari were chosen for porosity and permeability analysis: four close to the crater
455 lake (sites SP01, SP02, SP04, and SP07), two in a large gulley on the north-eastern wall
456 of the volcanic amphitheatre (sites SP06 and SP08), one near Troup Head (site SP05),
457 and one near Crater Bay (SP03) (localities shown in Figure 6). At each location, shovels
458 were used to expose up to several metres of fresh, vertical stratigraphy. Three of the
459 near-crater localities (SP01, SP02, and SP04) exposed a similar stratigraphy (Figure 6).
460 The base of these deposits, only exposed at trench SP02, consists of a yellow-coloured
461 ash/lapilli layer that contains a high percentage of large (~50 mm) lapilli fragments
462 overlain by a similarly coarse black-coloured horizon of ash/lapilli. Above this coarse
463 basal layer is a series of interbedded red- and grey/black-coloured deposits that likely
464 represent cyclic phreatic to phreatomagmatic eruptions. These layers contain a
465 noticeably smaller average particle size than the coarse basal layer. We interpret red-
466 and yellow-coloured layers to be more hydrothermally altered than those black in
467 colour. The deposits of the 2013 phreatic eruption mark the top of these crater floor
468 deposits. The final near-crater trench (SP07) is located in a gully (several metres deep)
469 draining southeast from Donald Duck crater. The flanks of this gully show signs of
470 outgassing activity and the deposits are hydrothermally altered as a result. The deposits
471 at this locality are yellow-grey in colour and contain few large lapilli fragments. The two

472 sites chosen on the north-eastern wall of the volcanic amphitheatre (SP06 and SP08)
473 were selected due to their differences in alteration. Further, these sites are both located
474 within the 2004 landslide deposit that has an anonymously low gas flux (*Bloomberg et*
475 *al.*, 2014). Site SP06 contains a hydrothermally altered grey/yellow-coloured ash/lapilli
476 debris flow deposit that contains large (~50 mm) angular lapilli fragments below a
477 laminated black/grey-coloured ash/lapilli deposit. Site SP08 comprises a grey-coloured
478 ash/lapilli debris flow deposit that contains large (~50 mm) angular lapilli fragments.
479 To measure characteristic reworked fluvial deposits not affected by hydrothermal
480 alteration, we selected two sites located far from the crater lake and the volcanic
481 amphitheatre rim (SP03 and SP05). Site SP03 contains a grey-coloured ash/lapilli
482 deposit that is overlain by a similar deposit that contains large (~50 mm) angular lapilli
483 fragments. Site SP05 consists of a brown-coloured ash/lapilli deposit.

484 A PL-300 soil permeameter (Umwelt-Geräte-Technik) was used to measure the
485 permeability of the layers of unlithified material (for more information see *Mayer et al.*,
486 2016b). Samples were first taken from the exposed stratigraphy using stainless steel
487 cylinders (of diameter 72 mm and length 61 mm; see inset in Figure 6). The
488 permeability could then be obtained using Darcy's law by measuring the volumetric flow
489 rate of air through the sample. An internal vacuum pump produces the inflow of air
490 through the sample, which is defined over a calibrated throat in the apparatus. The
491 pressure difference over the sample is recorded by a sensor, which provides the pressure
492 gradient of that flow. Comparison of the pressure gradient, in respect to a second
493 gradient over the calibrated permeability of the internal throat, enables the
494 determination of the volumetric flow rate of air through the sample and consequently
495 the estimation of its permeability. The permeability of at least two samples from each
496 distinguishable layer was measured (Table A3). We also measured the temperature of
497 each sample. The samples were then weighed and wrapped for transport.

Once back in the laboratory, the samples were oven-dried and their dry weight measured. The dry bulk density ρ_b could then be determined using the dry weight and the volume of the stainless steel cylinder. The solid density ρ_s (the density of the powder) was then measured using a helium pycnometer (Ultrapyc 1200e Quantachrome) and the total porosity determined using Equation 2. Finally, the water content of each sample was calculated using the *in-situ* and the oven-dry weights.

5.2 Laboratory materials and methods for the unlithified materials

Two unlithified samples were collected for permeability measurement in the laboratory. The first was a poorly sorted unlithified tephra deposit, the most abundant material of the crater fill (Figures 2 and 3g). The deposit (WI27; Figure 4i) was collected at a depth of one metre at the locality indicated in Figure 1. The deposit was first oven-dried. A portion of the deposit was then poured into the rubber jacket and permeability was measured using the above-described procedure. Due to the size of our rubber jackets (inner diameter of 20 mm), large lapilli were first removed. The ash/lapilli sample (WI27; Figure 4i) comprises mainly amorphous silica (59 wt.%), plagioclase (15 wt.%), pyroxene (9 wt.%), alunite (8 wt.%), and cristobalite (7 wt.%) (Table 1). The porosity was measured by determining the dry bulk density of the deposit within the jacket and the solid density (using the helium pycnometer); the total porosity could then be calculated using Equation 2. The unlithified ash deposit collected (WI28; Figure 4j) formed part of the blanket of fine ash that covers large parts of the crater floor near the crater lake (Figures 2 and 3h-i). The fine ash sample (WI27; Figure 4i), collected from Donald Duck crater (see Figure 1 for the collection locality), comprises mainly amorphous silica (52 wt.%), pyroxene (20 wt.%), plagioclase (18 wt.%), cristobalite (7 wt.%), and gypsum (3 wt.%) (Table 1). In order to measure the *in-situ* permeability, we carefully wrapped the sample upon collection to preserve the *in-situ* water content (which was calculated to be ~0.25 by measuring the *in-situ* weight and oven-dry weight

525 of a portion of the deposit). Once back in the laboratory, cylindrical samples (20 mm in
526 diameter and nominally 40 mm in length) were taken by pushing a cylindrical metal
527 sleeve into the sample. These cylindrical samples were then quickly and carefully
528 jacketed (using a rubber jacket) and loaded into the permeameter. Due to the low
529 permeability of the ash sample, the pressure decay method (*Brace et al*., 1968) was used
530 to determine their permeability. To do this, an initial increase (0.5 MPa) of the upstream
531 pressure was applied to the sample and the fluid inlet closed. The permeability was then
532 derived using the temporal decay of the upstream pressure. Owing to the delicate nature
533 of WI27 and WI28, permeability measurements were conducted at confining pressures
534 of 0.3 and 0.5 MPa, respectively.
535
536 **6. Results**
537
538 *6.1 Field porosity and permeability of the lithified materials*
539 Permeability as a function of dry bulk density for the 115 hand-sized sample
540 blocks is shown in Figure 7a (Tables A1 and A2). We find that the dry bulk density and
541 permeability of the samples varies between 1000 and 2000 kg/m^3 and between $\sim10^{-15}$
542 and $\sim10^{-11}$ m^2, respectively (Figure 7a). When dry bulk density is converted to total
543 porosity we find values between ~0.1 and ~0.6 (Figure 7b). We find no discernible
544 trends in the bulk density-permeability (Figure 7a) or porosity-permeability (Figure 7b)
545 data, although we note that the lava and lava breccia samples (black circles) are
546 typically denser/less porous than the ash tuffs (white circles) (Figure 7).
547
548 *6.2 Field porosity and permeability of the unlithified materials*
549 The calculated total porosity of the unlithified deposits is plotted as a function of
550 their stratigraphic depth in Figure 8a. We find that porosity ranges from ~0.25 to ~0.75.
551 There is no strong correlation between total porosity and the depth of the deposit (up to

552 a maximum depth of ~140 cm; Figure 8a). There is however a strong correlation
553 between water content (calculated using the *in-situ* and dry weight of the sample) and
554 depth (Figure 8b): water content increases linearly with depth. As a result, the air-filled
555 porosity in the deposits decreases as depth increases (Figure 8c). Based on these data
556 (Table A3), the water table within the crater-fill deposits at Whakaari is at a depth of
557 about 130-140 cm. We also note that the temperature of the deposit increases with
558 increasing depth, from ~22 °C at the surface to ~50-70 °C at a depth of ~100 cm (see
559 inset in Figure 8c). The data of Figure 8 are available in Table A3.

560 Since the gas moving through the sample can only travel through the air-filled
561 porosity on the timescale of the measurement, we have chosen to plot permeability as a
562 function of air-filled porosity (Figure 9a). We see that, generally, permeability increases
563 with increasing air-filled porosity. As a result, and although there is a lot of scatter,
564 permeability is seen to decrease with depth (Figure 9b). The data of Figure 9 are
565 available in Table A3.

566

567 *6.3 Laboratory porosity and permeability of the lithified materials*

568 Permeability as a function of connected porosity for the 136 20 mm-diameter
569 samples is shown in Figure 10 (Tables A4-A6). We find that the connected porosity and
570 permeability of the samples varies between ~0.1 and ~0.7 and between ~10^{-15} and ~10^{-11} m^2, respectively (Figure 10). If one considers the lava and lava breccias and the ash
572 tuffs separately, we find that, for both rock types, permeability increases as porosity
573 increases (Figure 10). In detail, increases in lava permeability are large as connected
574 porosity is increased when the porosity is low (less than ~0.15) and small as connected
575 porosity is increased when the porosity is high (greater than ~0.15) (Figure 10). All of
576 the lava breccia samples contain a porosity > 0.2 and therefore form part of the latter
577 trend. We also note that the jarosite (orange circles) and sulphur (green circles) crusts
578 do not plot within the broad porosity-permeability trend defined by the ash tuff

samples: the jarosite crust samples in particular were considerably more permeable than ash tuffs of a similar porosity (Figure 10; Table A6). The permeability of the prepared sulphur flow samples was too low for measurement in our benchtop permeameter (permeability < 10^{-18} m^2) (Table A6).

6.3.1 Influence of macrocracks on the permeability of lava

The presence of a macrocrack (parallel to the direction of flow) in samples of lava serves to greatly increase their porosity and permeability (Table A4). Porosity increased from 0.036 to between 0.092 and 0.112 when a macrocrack was present. Permeability increased from 1.6 × 10^{-16} m^2 (macrocrack-free sample) to 1.4 × 10^{-14} and 1.1 × 10^{-13} m^2 for the macrocracked samples containing porosities of 0.092 and 0.112, respectively (Table A4). We use here the two-dimensional model proposed by *Heap and Kennedy* (2016) to determine their fracture permeabilities k_f:

$$k_f = \frac{Ak_e - A_{intact} \cdot k_0}{A_{fracture}} \quad (3)$$

Where A, $A_{fracture}$ and A_{intact}, are the areas of the sample end face, the fracture, and the intact portion of the sample end face, respectively, and k_e and k_0 are the equivalent (i.e., the permeability of the fractured sample) and intact permeabilities, respectively. Assuming a constant throughgoing fracture width of 0.5 mm, we calculate fracture permeabilities of 4.3 × 10^{-13} and 3.3 × 10^{-12} m^2 for the macrocracked samples containing porosities of 0.092 and 0.112, respectively (Table A4).

6.3.2 Influence of gas elutriation pipes on the permeability of ash tuff

To assess the influence of gas elutriation pipes on the permeability of the ash tuffs, permeability was measured on samples of WI21b containing gas elutriation pipes orientated either parallel or perpendicular to the direction of fluid flow (Figure 11;

605 Table A5). Although the sample with the highest permeability (3. 1 × 10^{-15} m^2) contains
606 gas elutriation pipes parallel to flow, we note that two similarly prepared samples have
607 permeability values ~10^{-16} m^2 (Figure 11; Table A5). It is difficult therefore to draw firm
608 conclusions as to the influence of gas elutriation pipes on the permeability of the ash tuff
609 from these data.
610
611 6.3.3 Influence of confining pressure on permeability
612 The influence of confining pressure (up to 30 MPa) on the permeability of a lava
613 sample (WI20; without macrocracks) and an ash tuff sample (WI21b; parallel gas
614 elutriation pipes) is presented in Figure 12 (data available in Table A7). Assuming a
615 constant bulk density for WI20 and WI21 of 2500 and 1500 kg/m^3, respectively, the
616 depth at a pressure of 30 MPa was estimated using $P = \rho g z$ to be ~1.2 and ~2 km for
617 WI20 and WI21, respectively. The reduction of permeability with increasing pressure is
618 much higher for the lava than for the ash tuff sample (Figure 12). The permeability of
619 the ash tuff was reduced from 7.6 × 10^{-15} m^2 at a confining pressure of 1 MPa down to
620 4.7 × 10^{-16} m^2 at 30 MPa. In the same pressure range, the permeability of the lava
621 deposit was reduced from 1.0 × 10^{-16} to 2.4 × 10^{-17} m^2. In both cases, the largest
622 permeability decrease was seen as the confining pressure was increased from 1 to 2
623 MPa. Following this initial decrease, the permeability decreased more-or-less
624 monotonously with increasing confining pressure (Figure 12).
625
626 6.3.4 Pore throat diameter of lava and ash tuffs
627 The pore throat diameter distributions, as measured by mercury injection, for
628 the lava sample (WI20) and the four ash tuffs (WI21, WI22, WI23, and WI24) are
629 presented in Figure 13. For the lava we find that only 5% of the pore throats have a
630 diameter larger than 0.2 mm; the majority of the pore throats (95%) are between 0.2
631 and 0.004 mm in diameter. The most abundant pore throat diameter for WI20 is 0.006

632 mm. The pore throat diameter distributions for the ash tuffs are very different to that of
633 the lava: the ash tuffs contain a much larger proportion of larger pore throats (Figure
634 13). Indeed, pore throats greater than 100 μm were measured in the ash tuffs. The pore
635 throat diameter distributions for the different ash tuffs are quite similar, although we
636 note that WI24 contains a lower proportion of small (< 0.04 mm) pore throats than the
637 other ash tuffs. The most abundant pore throat diameters are 0.1, 0.006, 0.05, and 0.04
638 mm for WI21, WI22, WI23, and WI24, respectively (Figure 13).
639
640 *6.4 Laboratory porosity and permeability of the unlithified materials*
641 The total porosity of the unlithified ash/lapilli (dried) and the fine ash (dried)
642 were calculated to be 0.54 and 0.45, respectively. Since the *in-situ* water content of the
643 fine ash is ~0.25, the air-filled porosity of the *in-situ* deposit is estimated to be ~0.2. The
644 permeability of the unlithified ash/lapilli (dried) and the fine ash (*in-situ* water content
645 = ~0.25; air-filled porosity = ~0.2), as measured in the laboratory, were 3.36×10^{-12} and
646 4.50×10^{-19} m^2, respectively.
647
648 **7. Discussion**
649
650 *7.1 Laboratory versus field measurements*
651 The total porosity and permeability determined in the field is compared with
652 laboratory measurements on the samples cored from the same block in Figure 14. We
653 find that laboratory porosity is typically slightly higher than the porosity measured in
654 the field, but that there is no systematic variation with increasing porosity (Figure 14a).
655 It is likely that dry bulk density is overestimated using the field technique due to the
656 imbibition of water, an offset that could be corrected empirically (*Farquharson et al.*,
657 2015). However, estimates of permeability using the TinyPerm II unit over- or
658 underestimated the permeability of the measured rocks by two or in some cases three

659 orders of magnitude (Figure 14b). For the most part, the permeability measured by the
660 TinyPerm II unit overestimated the permeability; this is perhaps due to the fact that the
661 permeability of some blocks was too low to be measured by the TinyPerm II (although
662 the unit gives a value regardless). Overestimations could also be due to an imperfect seal
663 between the rock and the nozzle due to an uneven rock surface and/or due to the
664 presence of a low-permeability skin (although, as noted above, we tried to remove low-
665 permeability skins prior to measurement). It is clear from these data that, although the
666 TinyPerm II unit offers a quick and easy estimate of permeability, such estimates should
667 be groundtruthed by well-constrained laboratory data.
668
669 *7.2 Porosity and permeability relationships in the lithified materials*
670 Generally speaking, the permeability of porous media increases with increasing
671 connected porosity (e.g., *Bourbié and Zinszner*, 1985; *Wadsworth et al*., 2016). However,
672 the link between porosity and permeability is not straightforward, as permeability does
673 not strictly rely on porosity, but on the connectivity and geometry of the porosity (crack
674 porosity versus pore porosity, pore and crack geometries, pore and crack tortuosity,
675 amongst others). In other words, low-porosity rocks can have a high permeability, and
676 vice versa. Volcanic rocks in particular display a wide range of microstructure and
677 laboratory studies have exposed porosity-permeability relationships for a variety of
678 volcanic rocks (*Klug and Cashman*, 1996; *Saar and Manga*, 1999; *Rust and Cashman*,
679 2004; *Mueller et al*., 2005; *Wright et al*., 2009; *Farquharson et al*., 2015; *Kennedy et al*.,
680 2016; *Kushnir et al*., 2016; *Heap and Kennedy,* 2016). Few laboratory studies however
681 have measured the porosity and permeability of hydrothermally altered volcanic rocks
682 (e.g., *Siratovich et al*., 2014; *Mayer et al.,* 2016a; 2016b). Our study has shown that the
683 porosity-permeability relationships for the hydrothermally altered materials that form
684 Whakaari are complex (Figure 10). Due to the limitations of TinyPerm field

685 permeameter (Figure 14b), in the following discussion we will focus solely on
686 laboratory measurements of porosity and permeability (Figure 10).

687 We also highlight that the measurements of porosity and permeability provided
688 herein were determined using gas (helium and nitrogen, respectively). It is well known
689 that measurements of permeability will be influenced by the presence of clays (*Faulkner*
690 *and Rutter*, 2000; *Tanikawa and Shimamoto* 2009), which is the case for two of the
691 samples collected (WI23 and WI30; Table 1). The measurements of permeability
692 provided here will therefore overestimate the permeability of these samples to water,
693 since water will serve to swell the clays present within the rock and hence reduce the
694 permeability. However, it is unclear at present the influence of hydrothermal brines and
695 seawater on the permeability of clay-bearing rocks.

696 It is also important to note that laboratory measurements of permeability are
697 scale-dependent (*Brace*, 1984; *Clauser*, 1992; *Neuman*, 1994; *Heap and Kennedy*, 2016;
698 *Farquharson et al*., 2016). Due to the small size of laboratory samples, measurements of
699 permeability in the laboratory do not account for macroscopic features (such as
700 macroscopic fractures or bedding). They will therefore under- or overestimate the
701 equivalent permeability if the macroscopic feature provides a pathway or a barrier to
702 fluid flow, respectively.

703

704 7.2.1 Porosity and permeability relationships in the lavas and lava breccias

705 We find that a single power law cannot describe the porosity-permeability trend
706 for the lavas and lava breccias (Figure 10). While porosity-permeability relationships for
707 volcanic rocks have been classically described using a single power law model (e.g.,
708 *Mueller et al*., 2005), recent studies have invoked a double power law model
709 (*Farquharson et al*., 2015; *Heap et al*., 2015b; *Kushnir et al*., 2016; *Heap and Kennedy,*
710 2016). The double power law model consists of two discrete power laws that intersect
711 at a so-called "porosity changepoint" x^*. The use of two power laws in these studies, as

712 opposed to one, has been statistically verified using Bayesian Information Criterion
713 (BIC) analysis (e.g., *Main et al.,* 1999). The physical meaning of the porosity changepoint
714 is thought to represent a change in microstructure. Low-porosity volcanic rocks often
715 contain a poorly connected or tortuous network of pores, and fluids are often obliged to
716 travel through narrow microcracks that connect the pore network (*Heap et al.*, 2014;
717 *Farquharson et al.*, 2015; *Kushnir et al.*, 2016; *Heap and Kennedy,* 2016). Moderate- to
718 high-porosity volcanic rocks, by contrast, often contain a well-connected network of
719 large pores and channels (*Rust and Cashman*, 2004; *Wright et al.*, 2006; *Farquharson et*
720 *al.*, 2015; *Kennedy et al.*, 2016; *Kushnir et al.*, 2016; *Heap and Kennedy,* 2016). The
721 porosity changepoint in these studies lies within a narrow range of porosity: between
722 0.15 and 0.2 (*Farquharson et al.*, 2015; *Heap et al.*, 2015b; *Kushnir et al.*, 2016; *Heap and*
723 *Kennedy,* 2016). Applying the same BIC analysis to the lava and lava breccia data of this
724 study confirms that they are statistically better described by two power laws that
725 intersect at a changepoint porosity of ~0.14 (Figure 15), rather than a single power law.
726 The determined changepoint is similar to those found for extrusive andesites and
727 basaltic-andesites (*Farquharson et al.*, 2015; *Kushnir et al.*, 2016; *Heap and Kennedy,*
728 2016) and viscously densifying block-and-ash flow deposits (*Heap et al.*, 2015b). The
729 physical meaning of the porosity changepoint in the lavas and lava breccias from
730 Whakaari appears consistent with that described by these previous studies. Lava sample
731 WI20—which contains a porosity of ~0.06 (i.e., below the changepoint)—contains few
732 pores that are connected by a tortuous network of microcracks (Figure 4a). Indeed,
733 mercury injection analysis shows that the majority of the pore throats (95%) are
734 between 0.2 and 0.004 mm in diameter (i.e., microcracks connect the porosity; Figure
735 13) and the application of modest confining pressures significantly reduced the
736 permeability, interpreted as a consequence of the closure of compliant microcracks
737 (Figure 12; see also *Vinciguerra et al.,* 2005 and *Nara et al.,* 2011). By contrast, sample
738 WI-F-96 contains a very high porosity ~0.65 (i.e., above the changepoint) and contains a

739 network of presumably well-connected channels that are visible with the naked eye
740 (Figures A1 and A6).

741 We find that, despite the hydrothermal alteration of the lavas (Figures 4a, 4l, and
742 A6), their values of porosity and permeability are not dissimilar to those for unaltered
743 lavas (e.g., *Farquharson et al*., 2015; *Kushnir et al*., 2016; *Heap and Kennedy,* 2016).
744 However, we stress that alteration must greatly modify the porosity structure of a
745 material to greatly modify porosity and permeability. This is typically not the case for
746 the studied altered lava samples (Figures 4a, 4l, and A6). For example, we find that pore-
747 and fracture-filling precipitation is rare in the lavas collected (Figures A6-A7): a modest
748 volume of cristobalite (14 wt.%) and minor jarosite and gypsum precipitation is present
749 in sample WI20 (although the presence of pore-filling cristobalite may not decrease
750 permeability if associated with microporous diktytaxitic textures; *Kushnir et al*., 2016)
751 and kaolinite (10 wt.%) is present in sample WI30 (although it is not clear whether such
752 clays are associated with mineral replacement or pore- or crack-filling precipitation).
753 Indeed, lava sample WI20 can be classified only as *moderately* altered, since less than
754 half of the original mineral phases have been altered or replaced (BS5930, *1999*). We do
755 note however that hydrothermal alteration of the lava likely contributed to the growth
756 of the macrocracks that are commonly found within the lavas at Whakaari (e.g., Figure
757 4a); hydrothermal alteration has been previously shown to reduce material strength
758 (*Pola et al*., 2012; *Frolova et al*., 2014; *Wyering et al.*, 2014). We show here that such
759 macrofractures can increase sample permeability by a three orders of magnitude (Table
760 A4; Figure 15), in accordance with previous studies on the influence of macrofractures
761 in volcanic rock (*Nara et al*., 2011; *Heap and Kennedy*, 2016). An example of such a
762 fracture in the lavas at Whakaari is provided in Figure 16a. A second noteworthy
763 observation is that macrocracks within the lavas can be efficiently sealed with
764 hydrothermal precipitates (see the example in Figure 16b). Andesite blocks ejected from
765 the 1978 crater also contained 5-10 mm wide veins of alunite, anhydrite, and Al-rich

766 chlorite (*Hedenquist et al*., 1993). Progressive precipitation within fractures will greatly
767 reduce their permeability (*Edmonds et al*., 2003; *Griffiths et al*., 2016).

768 The high permeability of the fractures within low-permeability lava ($\sim 10^{-13}$ to
769 $\sim 10^{-12}$ m^2) coupled with the presence of fracture-filling precipitation suggests that such
770 fractures are preferentially used as pathways for hydrothermal fluids. Therefore, high-
771 permeability fractured (altered) lavas could be modified to low-permeability lavas
772 containing sealed fractures over time, providing that the fluid temperature and
773 composition (including pH) support mineral precipitation.

774

775 7.2.2 Porosity and permeability relationships in the tuffs and crusts

776 The porosity-permeability relationship for the ash tuffs is considerably more
777 scattered than that for the lavas and lava breccias, although there is a general trend of
778 decreasing permeability with decreasing porosity (Figure 15). We highlight that the
779 observation of a trend in these data is only made possible by the large number of
780 datapoints (n = ~100; Tables A5-A6), a prerequisite for understanding relationships in
781 rocks with variable microstructures due to variable alteration styles and intensities. We
782 observe no porosity changepoint in the ash tuff data. The absence of two distinct
783 porosity/permeability trends is likely due to the absence of two distinct microstructural
784 groups in the ash tuff samples (i.e., microcracks and few pores versus a well-connected
785 pore network). If microcracks were present in all of the ash tuff samples, it would serve
786 to increase the permeability of the low-permeability samples, but would not
787 significantly change the permeability of the high-permeability samples (see also *Heap*
788 *and Kennedy*, 2016), thus potentially creating a changepoint. Microcracks were not
789 observed during our SEM analysis of the ash tuff samples (Figures 4b-f) and mercury
790 injection analysis showed that pore throats can be as large as ~100 μm (i.e., pores;
791 Figure 13). The modest decrease in permeability as confining pressure is increased is
792 further evidence of the absence of microcracks in the ash tuff samples (Figure 12).

However, we highlight that a changepoint can exist for granular, microcrack-free materials (*Bourbié and Zinszner*, 1985; *Heap et al.*, 2015b). It is possible therefore that a microstructural changepoint could exist for the ash tuffs of this study at a lower porosity (~0.1-0.15), in accordance with those found for sandstone (*Bourbié and Zinszner*, 1985) and welded pyroclastic deposits (*Heap et al.*, 2015b). This assertion is supported by the very low porosity and permeability of the highly cemented sulphur flow samples (WI29; Table A6) which, if plotted on Figure 15, would presumably not follow the single power law trend defined by the measured ash tuff samples. However, based on our data (Figure 15), low-porosity and low-permeability ash tuffs at Whakaari are likely rare and potential restricted to vent-proximal deposits cemented by sulphur.

Despite the trend of decreasing permeability with decreasing porosity, the permeability of the ash tuff can vary by up to five orders of magnitude for a single value of porosity (Figure 15). This is due to the considerable microstructural variability between the samples (particle size, pore size, amongst others; Figures A8-11). If we first consider alteration style, we find that white-coloured ash tuff samples (their white colour is indicative of alunite, a sulphate that is found as a replacement mineral and as a pore-filling precipitate; Figure 5; *Heap et al.*, 2015a; *Mayer et al.*, 2015) are typically of lower porosity and permeability (white circles in Figure 15) than grey-, brown-, and red/purple-coloured ash tuff samples (samples that do not contain alunite; grey circles in Figure 15). It is possible that porosity and permeability were reduced in these samples due to the precipitation of pore-filling alunite, a consequence of their exposure to acid-sulphate fluids. Alunite precipitates from low-pH solutions (*Brown*, 1978; *Ece et al.*, 2008), typically between 2.5 and 3.0 (*Brown*, 1978), and requires the formation of sulphuric acid either by (1) atmospheric oxidation of iron sulphides (supergene environment), (2) atmospheric oxidation near the water table of H_2S from deeper boiling fluids (steam-heated hydrothermal environment) and (3) disportionation of SO_2 to H_2SO_4 and H_2S from a condensing magmatic vapour plume (magmatic hydrothermal

820 environment) (*Rye et al.*, 2002; *Mutlu et al.*, 2005; *Zimbelman et al.*, 2005; *Ece et al.*,
821 2008; *Pirajno*, 2009). Therefore, progressive alunite precipitation could reduce porosity
822 and permeability in accordance with the porosity-permeability trend shown in Figure
823 15, although we note that tuffs without alunite alteration can also be of low porosity and
824 permeability. While the observation that the density of rocks within the Biga Peninsula
825 (Turkey) increases with alunite content (*Ece et al.*, 2008) supports such a hypothesis,
826 firm conclusions cannot be drawn without undertaking laboratory-controlled
827 precipitation experiments.

828 We further note that some alunite-bearing samples contain very small pores (i.e.,
829 pores that cannot be seen with the naked eye; WI-F-3, WI-F-52, WI-F-110, and WI-F-
830 112; Figures A8-11) and that these samples all have very low permeabilities of $\sim 10^{-17}$
831 m^2 (Table A5). It is likely that the pore radii in these samples have been dramatically
832 reduced by pervasive alunite precipitation, explaining their low permeability (although
833 a high density of very small pores allows the rock to maintain a high porosity). Such low-
834 permeability layers can also exist as thin (~2-4 mm) layers (as is the case for WI-F-4;
835 Figure A8). The thin layer in samples of WI-F-4, orientated perpendicular to the
836 measurement of permeability, dramatically reduced sample permeability: the
837 permeability of these samples is also $\sim 10^{-17}$ m^2 (Table A5).

838 Therefore, shallow tuffs that exist within pathways for hydrothermal fluids may
839 be of lower porosity and permeability than those shielded from acid-sulphate fluids,
840 providing that the fluid temperature and composition (including pH) support mineral
841 precipitation. Near active vents and fumaroles, where the pH may preclude alunite
842 precipitation (pH can be close to unity; *Giggenbach et al.*, 1993), the cementation of
843 tephra deposits and tuffs by sulphur can effectively destroy porosity and permeability
844 (as is the case for the sulphur flow sample WI29; Table A6; see also *Harris and*
845 *Maciejewski*, 2000; *Christenson et al.*, 2016).

Macroscopic textures add another degree of complexity. We observe gas elutriation pipes (e.g., sample WI21; Figures A8-11) and bedding (e.g., samples WI22 and WI23; Figures A8-11) in some of the samples collected. Although the influence of bedding-perpendicular gas elutriation pipes on permeability is unclear with the available data (Figure 11), we anticipate that the observed bedding will promote a permeability anisotropy within the ash tuff deposits (not tested systematically here due to the limited size of the blocks collected), especially if adjacent interbedded layers or laminations have disparate values of porosity and permeability (e.g., WI-F-4; Figure A8). Bedding-induced permeability anisotropy will favour the lateral movement of fluids over the vertical movement of fluids.

The porosity and permeability of the crust (jarosite and sulphur) samples (Figure A12) is distinct from the ash tuffs (Figure 15; Tables A5-A6). The jarosite crust samples in particular are much more permeable (about 5 orders of magnitude) than ash tuffs of a similar porosity. In terms of porosity-permeability, the crust samples are similar to porous sandstones. For example, the permeability of Berea sandstone (porosity = 0.21) is about 5.0×10^{-12} m^2 (*Zhu and Wong, 1997*). The higher permeability of the crust samples and the ash tuff samples can be explained by their larger pore size compared to the ash tuffs (Figure 4). The presence of larger pores is likely due to the fact that these surficial deposits are yet to undergo compaction as a result of burial by more recent tephra deposits.

7.3 Porosity and permeability relationships in the unlithified materials

The outgassing of magmatic volatiles and the movement of hydrothermal fluids through and within the shallow crater floor must rely on the permeability of the surficial, unlithified ash/lapilli deposits. When dry, the unlithified crater-fill deposits have a high permeability of $\sim 10^{-12}$ m^2 (measured in the laboratory). Under *in-situ* (i.e., partially-saturated) conditions, we measured permeabilities between $\sim 10^{-15}$ and $\sim 10^{-12}$

873 m^2 (Figure 9; Table A3) for the unlithified materials of the crater floor, values not
874 dissimilar to the ash tuffs (Figure 15). Samples at or very close to complete saturation (>
875 1 m depth) had permeabilities too low to be measured by the PL-300 soil permeameter
876 (Table A3). We find that permeability decreases with the available air-filled porosity and
877 with depth (Figure 9). It is important to note that the *in-situ* values of field permeability
878 for the unlithified deposits are relevant for gases (e.g., CO_2) moving through deposits
879 partially saturated with aqueous fluids; these values likely therefore considerably
880 underestimate the permeability of these deposits to aqueous solutions.

881 To understand the role of texture on the permeability of the unlithified deposits,
882 we plot those deposits containing large lapilli fragments as squares whilst deposits
883 without large lapilli fragments are plotted as circles (Figure 17). We find that there is no
884 correlation between the presence/absence of large lapilli and porosity-permeability
885 (Figure 17). We also use these data to assess the impact of alteration on the porosity and
886 permeability values of these unlithified deposits. The red-coloured deposits—
887 interpreted here as high alteration layers—are plotted as red symbols, the highly
888 altered deposit at SP07 (Figure 6) is plotted as a yellow symbol, and the largely
889 unaltered deposits of trench SP05 and SP08 (Figure 6) are shown as grey symbols in
890 Figure 17. In highlighting these data we see that there is no obvious correlation between
891 alteration and porosity and permeability (Figure 17). It follows that, since we see no
892 evidence of compaction (Table A3), permeability to gas in these deposits simply
893 decreases with depth due to the increase in water saturation with depth (Figures 8 and
894 9). To modify permeability of a material, the alteration must modify the structure of the
895 porosity (e.g., through dissolution, precipitation, alteration-induced cracking). However,
896 if the deposit remains unlithified, the alteration must have simply resulted in
897 devitrification, oxidation, or mineral replacement of the ash and lapilli particles; there
898 was therefore no change to the interstitial void space, and therefore no change to the
899 porosity or permeability. However, permeability may be reduced if the alteration results

900 in the formation of clay minerals. Therefore, despite the absence of a correlation
901 between alteration and porosity/permeability in our data (Figure 17), we do not
902 preclude here alteration-induced changes to porosity/permeability in the unlithified
903 deposits at Whakaari.

904 Values of permeability between ~10^{-15} m^2 and ~10^{-12} m^2 were measured for the
905 unlithified crater-fill deposits (Figure 9; Table A3). Therefore, the circulation and
906 passage of fluids within and through the deposits of the crater floor should be largely
907 unimpeded. However, gases may struggle to quickly negotiate through deeper deposits
908 that are close to complete water saturation. Indeed, samples at or very close to complete
909 saturation (> 1 m depth) had permeabilities too low to be measured by the PL-300 soil
910 permeameter (Table A3). The movement of fluid (both gases and aqueous solutions)
911 will be strongly inhibited by the layers of partially saturated fine ash however (such as
912 that near Donald Duck and Noisy Nellie craters; Figures 3h-i), which has an *in-situ*
913 permeability of ~10^{-19} m^2 (measured in the laboratory). Blankets of fine ash within the
914 unlithified crater floor deposits will create a permeability anisotropy and are likely to
915 strongly inhibit the vertical movement of hydrothermal fluids.
916
917 **8. Conclusions and implications for Whakaari (White Island volcano)**

918 Understanding the eruptive behaviour of, and modelling unrest at, Whakaari
919 rests on a detailed comprehension of the permeability of the materials that form and
920 exist within the crater. We find that the assembled products at Whakaari vary
921 considerably in terms of porosity and permeability: porosity ranges from ~0.01 up to
922 ~0.7 and permeability spans eight orders of magnitude (from ~10^{-19} to ~10^{-11} m^2). This
923 variability is due to the variable rock types forming the flanks of the volcano and filling
924 the craters (tuffs, lavas, lava breccias, and unlithified tephra), their varied
925 microstructures, and their varied hydrothermal alteration. As a result, the spatial
926 distribution of the assembled volcanic materials is of paramount importance in

927 deciphering fluid flow in active volcanic hydrothermal systems. To this end, we have
928 constructed a cartoon cross section in which we capture the salient features of our
929 study, presented as Figure 18.

930 The chief lithologies at Whakaari are tuffs, lavas and lava breccias, and crater-
931 filling unlithified tephra (Figures 2, 3, and 18). The crater-filling tephra has a relatively
932 high permeability ($\sim 10^{-15}$ to $\sim 10^{-12}$ m^2), and is therefore unlikely to impede the
933 movement of fluids within the shallow crater (Figure 18, item 1), as evidenced by crater
934 floor gas flux measurements (*Bloomberg et al.*, 2014). Permeability in these unlithified
935 deposits may also be enhanced by vertical gas elutriation pipes (Figure 4c; Figure 18,
936 item 2). However, we highlight that bedding-induced permeability anisotropy (Figures
937 A8-11; Figure 18, item 3) and well-sorted layers of fine ash with a low permeability
938 (WI28 $\sim 10^{-19}$ m^2; Figure 3h and 3i; Figure 18, item 4) may impede and prevent vertical
939 fluid movement, respectively. We also note that permeability to gases will likely
940 decrease with depth (in the first few meters) in the unlithified crater-fill due to the
941 increase in water content, and therefore decrease in air-filled porosity, as depth
942 increases (Figures 8 and 9). While mineralogical transformations are unlikely to
943 influence porosity and permeability (Figure 17), cementation or clay formation will
944 likely result in reductions in tephra permeability. In particular, cementation of near-vent
945 tephra with sulphur (Figure 3e and 3f), where the pH is too high for alunite precipitation
946 (*Giggenbach et al.*, 2003), results in the destruction of porosity and permeability, both
947 horizontally as subcrater layers (*Christenson et al.*, 2016) and vertically as fumaroles
948 (sulphur flow sample WI29 contains a porosity of ~0.01 and a permeability < 10^{-18} m^2;
949 Figure 18, item 5). Near-vent cementation of tephra and tuffs with sulphur could
950 therefore lead to the clogging of active vents or time variable prevention of lateral
951 and/or vertical fluid movement (see also *Harris and Maciejewski*, 2000; *Mayer et al.*,
952 2016b; *Christenson et al.*, 2016).

953 The tuffs—formed by the consolidation and cementation of tephra deposits—
954 are typically porous (porosity = 0.3-0.7), although their permeability can range from
955 $\sim 10^{-17}$ to $\sim 10^{-12}$ m^2 (Figure 15). Tuffs are found forming the crater wall (although the
956 dominant lithology is lava/lava breccia; Figures 2, 3, and 18) and presumably comprises
957 the deep main crater fill (Figure 18), as can be seen in ballistics from recent eruptions.
958 As for the crater-fill tephra, bedding-induced permeability anisotropy and well-sorted
959 layers of fine ash tuff with a very low permeability may impede or restrict the vertical
960 movement of fluids (Figure 18, item 6) and vertical gas elutriation pipes may assist
961 vertical fluid movement (Figure 18, item 4). A notable observation is that the white-
962 coloured ash tuffs (an alteration colour associated with alunite) contain the lowest
963 porosities and have the lowest permeabilities (Figure 15). Therefore, hydrothermal
964 alteration of the ash tuffs in shallow zones (alunite is formed through the oxidation of
965 H_2S from deeper boiling fluids) that host or have hosted acid-sulphate hydrothermal
966 fluids can result in reductions in porosity and permeability through the precipitation of
967 pore-filling alunite (Figure 18, item 7), providing that the fluid temperature and
968 composition (including pH) support mineral precipitation. Hydrothermal alteration
969 deeper in the crater could also result in modifications to permeability (e.g., dissolution,
970 clay formation, amongst others; Figure 18, item 8).

971 The crater walls chiefly comprise lavas and lava breccias (Figures 2 and 3).
972 Discontinuities at the crater margin serve as a passageway for hydrothermal fluids and
973 feed the numerous active fumaroles, boiling mud pools, and springs for acid streams
974 (Figures 2, 3, and 16a; Figure 18, item 9) (*Bloomberg et al*., 2014). The porosity of the
975 lavas and lava breccias at Whakaari ranges from ~0.05 up to ~0.7, and permeability
976 ranges from $\sim 10^{-16}$ to $\sim 10^{-12}$ m^2 (Figure 15). Notably, we find that (1) the lava breccias
977 are significantly more permeable than the coherent lavas (Figure 15) and, (2)
978 macroscopic fractures within the lava samples (Figure 16a) increase sample
979 permeability by up to three orders of magnitude (Figure 15; Table A4). As a result, fluids

travelling through the crater walls (hydrothermal fluids and seawater; Figure 18) will likely negotiate through a combination of fractures within the lava (Figure 18, item 10) and the permeable lava breccia (Figure 18, item 11). The ingress of seawater into the hydrothermal system will result in the mixing of hydrothermal fluids and seawater (Figure 18, item 12). While the passage of hydrothermal fluids can weaken the lava and promote the growth and widening of fractures through alteration (e.g., mineral replacement and/or dissolution; Figure 16a), hydrothermal fluids can also seal fractures through precipitation (Figure 16b; *Hedenquist et al*., 1993). In zones where precipitation dominates over dissolution (a function of the fluid temperature and composition, including pH), the sealing of fractures will significantly reduce permeability (*Griffiths et al*., 2016; Figure 18, item 13), transforming a zone of high-permeability into a zone of low-permeability. The mixing of hydrothermal fluids and seawater can also result in mineral precipitation (such as anhydrite) and reductions to permeability (*Kawada and Yoshida*, 2010). Fracture pathways within the crater wall may also become clogged with sulphur precipitation (Figure 18, item 14). Finally, our data have shown that an increase in effective pressure (i.e., depth) will significantly reduce the permeability of the microfractured lava (Figure 12). The permeability of macrofractures will also be reduced at depth (*Nara et al*., 2011). As a result, fluids may find it increasingly difficult to find an escape route into the crater wall as depth is increased (Figure 18, item 15).

As outlined above, hydrothermal alteration typical of a volcanic hydrothermal system can result in increases (due to alteration-induced weakening and fracturing) and decreases (due to hydrothermal precipitation) to permeability. Importantly, a decrease in permeability, be it due to fracture sealing in the lava, pore-filling alunite precipitation, cementation by sulphur, and/or very low permeability layers (Figure 18), can result in pore pressure augmentation (*Christenson et al*., 2010; *Heap and Wadsworth*, 2016). An increase in pore pressure could jeopardise the stability of the volcanic slopes (*Day*, 1996; *Voight and Elsworth*, 1997; *Reid et al., 2001; Reid*, 2004; *Moon et al*., 2009), result

1007 in seismicity (*Nishi et al*., 1996; *Sherburn et al*., 1998; *Chardot et al*., 2015), and/or drive
1008 the wide variety of eruptions observed at Whakaari (e.g., *Houghton and Nairn*, 1991;
1009 *Mayer et al*., 2015). Indeed, an increase in pore pressure due to the hydrothermal
1010 system was thought responsible for the unrest between 2002-2006 and 2007-2009
1011 (*Fournier and Chardot*, 2012), although we note that lake level variations are likely to
1012 have significantly modified the pore fluid pressure within the system during these
1013 intervals (*Christenson et al*., 2016).

1014 The reduction in permeability may also encourage changes to the preferred
1015 pathways for hydrothermal fluid circulation. This is exemplified by the numerous past
1016 and present vents, fumaroles, and craters that pepper the main crater floor and the base
1017 of the slopes of the volcanic amphitheatre at Whakaari (Figures 2 and 3) and highlights
1018 the constantly evolving and unpredictable nature of hydrothermal volcanic systems (see
1019 also *Harris and Maciejewski*, 2000). Changes to hydrothermal circulation will also
1020 expose new tephra and tuffs to alunite, clay, and sulphur alteration/precipitation. The
1021 exposure of new materials to porosity and permeability reducing alteration could
1022 therefore result in a reduction of the equivalent permeability of the system over time,
1023 thereby increasing the potential for pore pressure augmentation and the associated
1024 hazardous consequences.

1025 The primary goal of this contribution was to produce a very large dataset to
1026 inform future modelling efforts. The permeability of the materials within active volcanic
1027 hydrothermal systems is, for example, required to understand and accurately model the
1028 outgassing of magmatic volatiles from the magma-filled conduit (*Collombet*, 2009;
1029 *Collinson and Neuberg*, 2012), subsurface hydrothermal activity and therefore volcanic
1030 unrest (*Hurwitz et al*., 2007; *Peltier et al*., 2009; *Todesco et al*., 2010; *Christenson et al*.,
1031 2010 *Fournier and Chardot*, 2012), gas monitoring (*Bloomberg et al*., 2014; *Peiffer et al*.,
1032 2014), and volcano seismicity (*Leet*, 1988; *Nishi et al*., 1996; *Sherburn et al*., 1998; *Bean*
1033 *et al*., 2014; *Chardot et al*., 2015). For example, *Fournier and Chardot* (2012) show, using

1034 a thermo-poro-elastic model, that increases in pore pressure at depth were likely
1035 responsible for recent (2002-2006 and 2007-2009) episodes of ground deformation at
1036 Whakaari. The model of *Fournier and Chardot* (2012) assumes an isotropic value
1037 permeability of 10^{-15} m^2 and, while these authors concede that the assumption of a
1038 permeability isotropy is an oversimplification, our study—which shows that
1039 permeability spans eight orders of magnitude (from $\sim10^{-19}$ to $\sim10^{-11}$ m^2) and is
1040 complicated by numerous spatial and temporal considerations (summarised in Figure
1041 18)—highlights the challenge presented for the construction of more complex models.
1042 Further, we stress that the construction of such models will require an improved
1043 understanding of the subsurface stratigraphy, hydrogeology, and geochemical
1044 composition of the hydrothermal fluids at Whakaari.

1045 Our study provides the most comprehensive dataset for the porosity and
1046 permeability of the materials that comprise a volcanic hydrothermal system to date.
1047 Although our study highlights an extreme variability in these parameters, we anticipate
1048 that these data will allow for a better understanding of the behaviour and evolution of
1049 volcanic hydrothermal systems worldwide.

1050

1051 **Acknowledgements**

1052 The authors of this study acknowledge two Hubert Curien Partnership (PHC)
1053 grants: a Dumont d'Urville grant (number 31950RK) and a Procope grant (number
1054 332065SG) funded and implemented by the New Zealand Ministry of Business,
1055 Innovation and Employment (MBIE), the Royal Society of New Zealand, the Deutscher
1056 Akademischer Austauschdienst (DAAD) in Germany, and the Ministry of Foreign Affairs
1057 (MAEDI) and the Ministry of Higher Education and Research (MENESR) in France. The
1058 first and third authors also acknowledge funding from an Initiative d'Excellence (IDEX)
1059 "Attractivité" grant (VOLPERM) and "Contrats doctoraux" grant, respectively, both
1060 funded by the University of Strasbourg. We acknowledge Catalyst Fund project "Energy

straight from magma", funded and implemented by the Royal Society of New Zealand and the New Zealand Ministry of Business, Innovation and Employment (MBIE). Funding for B. Kennedy was additionally provided by Marsden Fast Start (09-UO-017C) grant. B. Kennedy and Y. Lavallée thank the international science linkage funds from Royal Society of New Zealand (ISAT E613), the German Aerospace Centre (DLR) and the Federal Ministry of Education and Research (BMBF) (NZL 09/17). D. B. Dingwell acknowledges the ERC advanced grant "EVOKES" (explosive volcanism in the earth system: experimental insights, project number 247076). B. Scheu and K. Mayer acknowledge funding from the European Union's Seventh Program for research, technological development, and demonstration under grant agreement No 282759 (VUELCO). Y. Lavallée acknowledges ERC starting grant "SLiM" (Strain Localisation in Magmas, project number 306488). The mercury porosimetry was performed at the University of Aberdeen and thanks go to Dave Healy and Colin Taylor. We gratefully acknowledge B. Scott, S. Bloomberg, A. Mazot, and N. Win for field assistance. The Buttle Family, Pee Jay Tours, and the New Zealand Royal Air Force, in conjunction with GNS Science, provided field access. The comments of two anonymous reviewers improved the clarity of this manuscript.

Author contributions

M.J. Heap led the project and wrote the manuscript. Field work and sample collection was carried out by M.J. Heap, B.M. Kennedy, J.I. Farquharson, K. Mayer, M. Letham-Brake, B. Scheu, Y. Lavallée, and P. Siratovich. Laboratory measurements of permeability were collected and analysed by J.I. Farquharson, M.J. Heap, and T. Reuschlé. The permeability at different confining pressures was performed and analysed by T. Reuschlé. J. Ashworth and J.I. Farquharson collected and analysed the field data for the lithified rocks. K. Mayer and B. Scheu collected the field data for the unlithified deposits, which was analysed by K. Mayer. H.A. Gilg performed and analysed all of the XRPD data.

M.J. Heap and B.M. Kennedy conducted the SEM work. J.I Farquharson performed the Bayesian Information Criterion (BIC) analysis. The cross section was constructed by B.M. Kennedy, with help from M.J. Heap. All authors had a hand in the interpretation of the data and the writing of the manuscript.

1093 **Table 1**. X-ray powder diffraction (XRPD) analysis showing the quantitative bulk
1094 mineralogical composition of the nine lithified blocks and the two unlithified samples
1095 chosen for additional analyses. Values are in wt.%.
1096

Sample name	WI20 WI20c	WI21 WI21b	WI22	WI23	WI24	WI25	WI26	WI27	WI28	WI29	WI30
Rock type	Lava	Ash tuff	Ash tuff	Ash tuff	Ash tuff	Jarosite crust	Sulphur crust	Ash lapilli	Ash	Sulphur flow	Lava breccia
(K, Na)-Alunite	-	32 ± 3	6 ± 3	25 ± 3	1 ± 1	-	-	8 ± 2	-	1 ± 0	-
Jarosite	3 ± 1	-	-	4 ± 1	4 ± 1	25 ± 5	-	-	-	-	1 ± 0
Anhydrite	-	-	-	-	-	-	-	-	-	-	1 ± 0
α-Sulphur	-	-	-	-	-	-	46 ± 5	-	-	99 ± 0	-
Gypsum	4 ± 1	1 ± 1	1 ± 1	-	-	-	-	2 ± 1	3 ± 1	-	-
Amorphous phases (volcanic glass, opal-A)	14 ± 5	66 ± 6	90 ± 3	68 ± 4	92 ± 2	37 ± 5	44 ± 5	59 ± 5	52 ± 5	-	72 ± 4
Kaolinite	-	-	-	2 ± 2	-	-	-	-	-	-	10 ± 2
Cristobalite	17 ± 4	1 ± 1	3 ± 1	1 ± 1	2 ± 1	4 ± 1	1 ± 1	7 ± 1	7 ± 1	-	3 ± 2
Quartz	-	< 1	< 1	< 1	1 ± 1	1 ± 1	-	-	-	-	1 ± 0
Pyroxene	10 ± 2	-	-	-	-	22 ± 4	4 ± 3	9 ± 2	20 ± 4	-	3 ± 1
Plagioclase	37 ± 3	-	-	-	-	10 ± 3	5 ± 3	15 ± 2	18 ± 3	-	8 ± 3
Hematite	1 ± 1	-	-	-	1 ± 1	-	-	-	-	-	1 ± 0
K-Feldspar	14 ± 2	-	-	-	-	-	-	-	-	-	-

1097

Figure captions

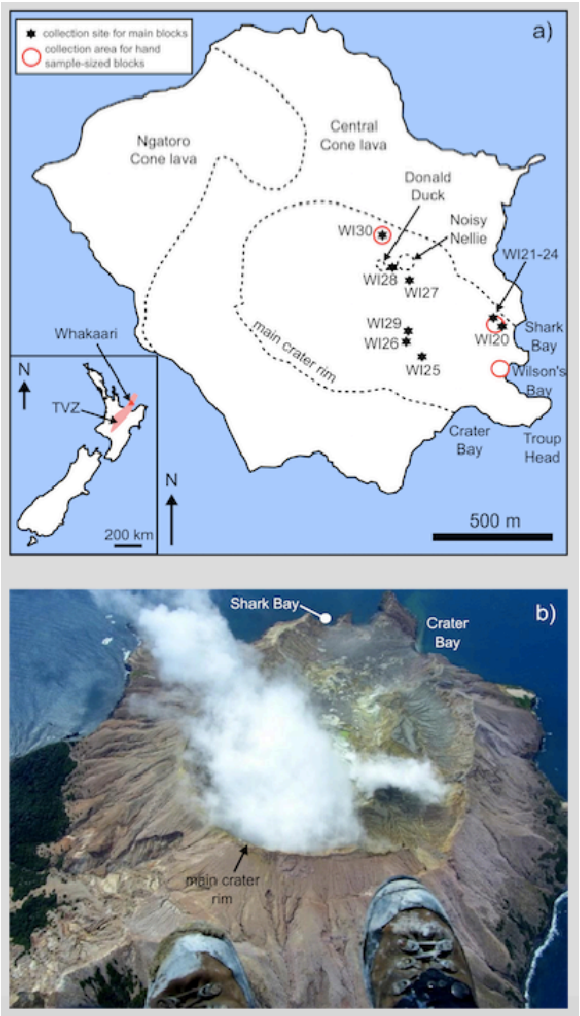

Figure 1. Whakaari (White Island volcano). (a) Map of Whakaari showing the locations of the collection sites for the lithified materials. The collection areas for the hand-sized sample blocks are indicated by the red circles. The collection sites for the nine main blocks of this study (and the two unlithified materials WI27 and WI28) are indicated by the black stars. The inset shows a map of New Zealand showing the location of the Taupo Volcanic Zone (pink area) and Whakaari volcano (red triangle). (b) Aerial photograph of Whakaari taken looking east-southeast.

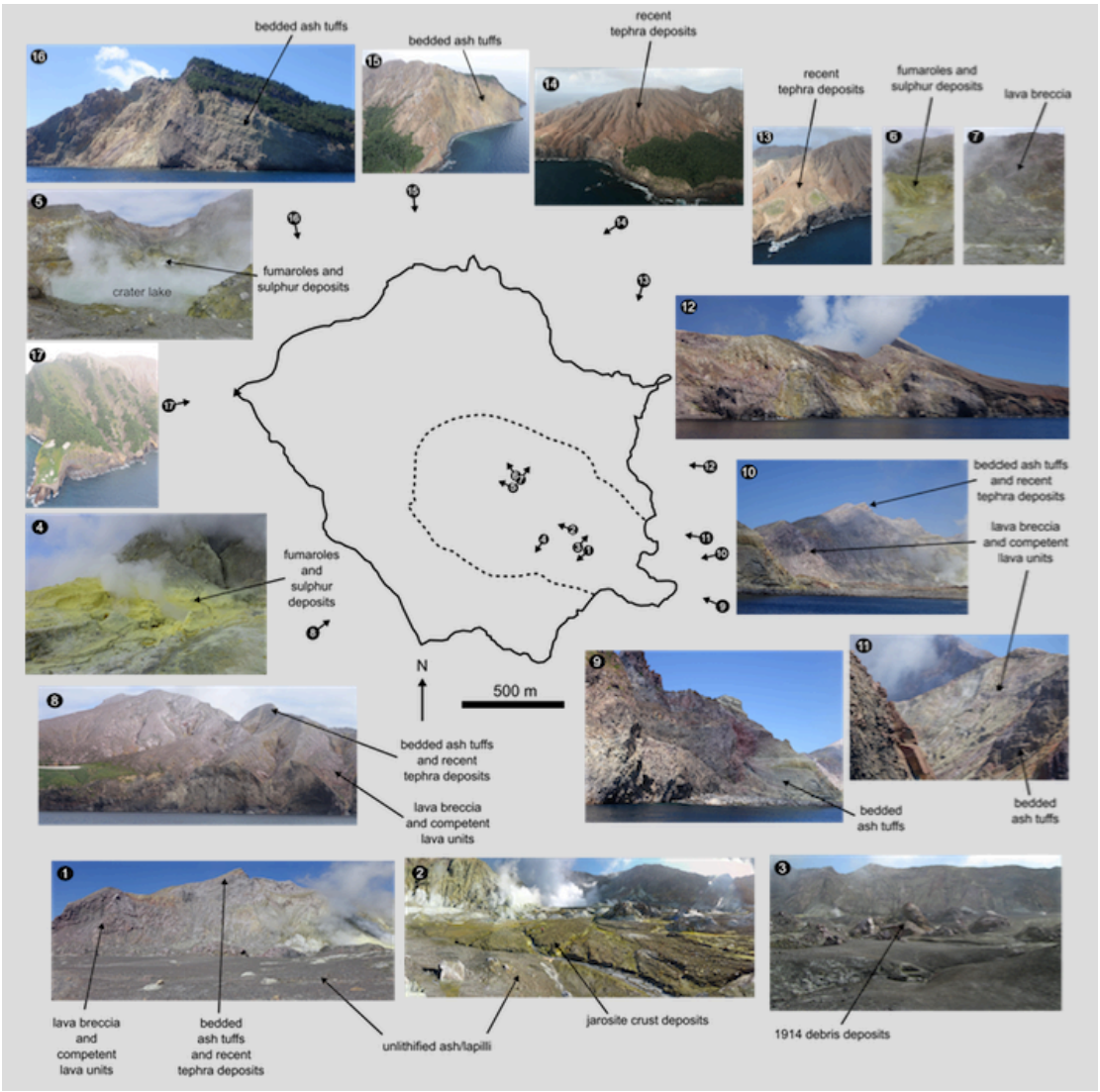

Figure 2. Reconnaissance by land, sea, and air. Map of Whakaari (centre) surrounded by photographs of the volcanic island. The position from which each photograph was taken, and the direction of view, is indicated by the numbers and arrows. Prominent rock types are labelled on the photographs.

Figure 3. Photographs showing the sites at which the nine lithified blocks of this study (and the two unlithified materials) were collected. The location of the collection sites are indicated on the map in Figure 1.

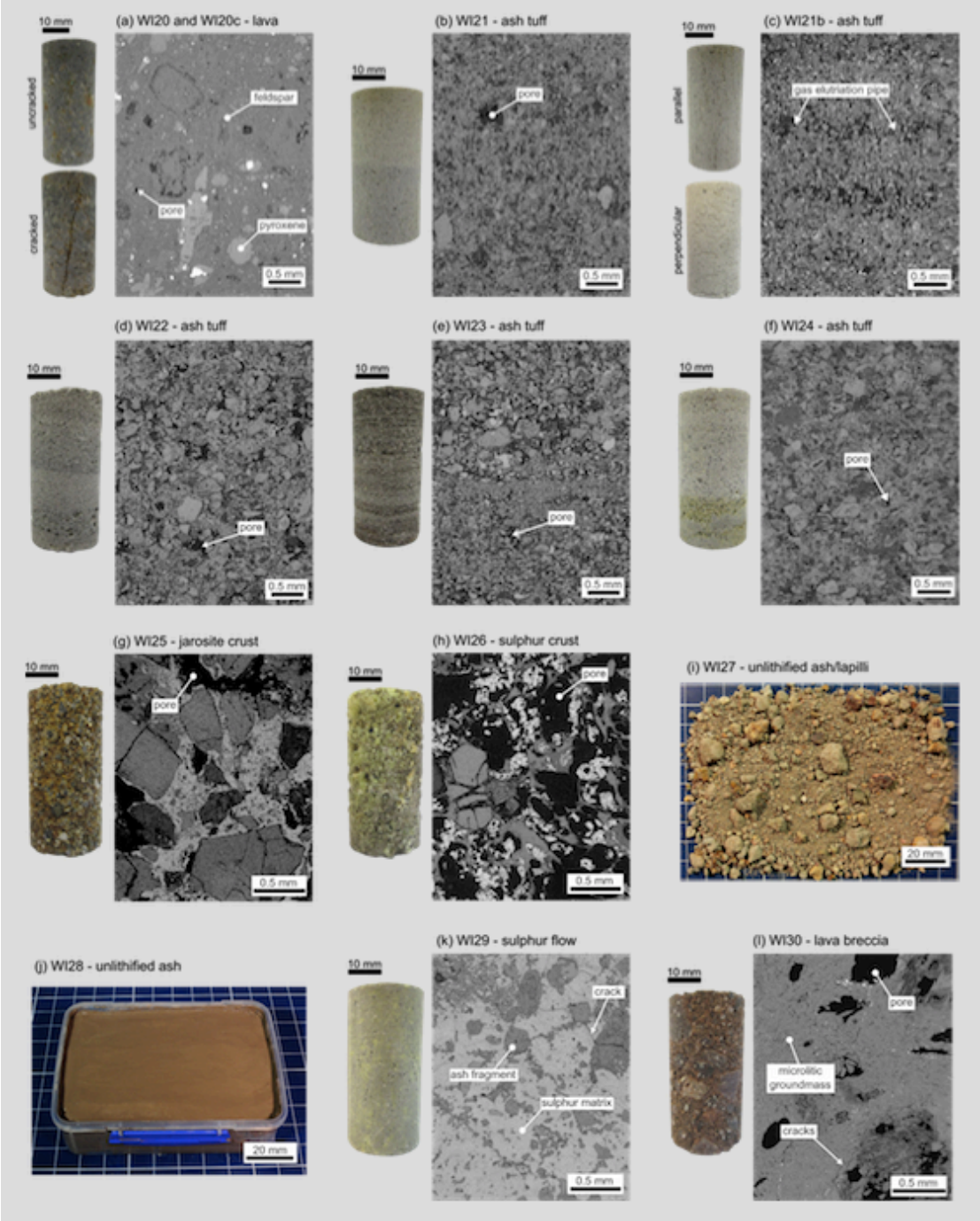

1123

1124 **Figure 4**. Photographs and scanning electron microscope (SEM) images of the nine main
1125 blocks of this study (and the two unlithified materials). (a) Macrocracked and uncracked
1126 lava WI20. (b-f) Ash tuff WI21, WI22, WI23, and WI24. (g) Jarosite crust WI25. (h)
1127 Sulphur crust WI26. (i) Unlithified ash/lapilli WI27. (j) Unlithified ash WI28. (k) Sulphur
1128 flow WI29. (l) Lava breccia WI30. Collection sites for each material are indicated in
1129 Figure 1 and photographs of the collection sites are provided in Figure 3.

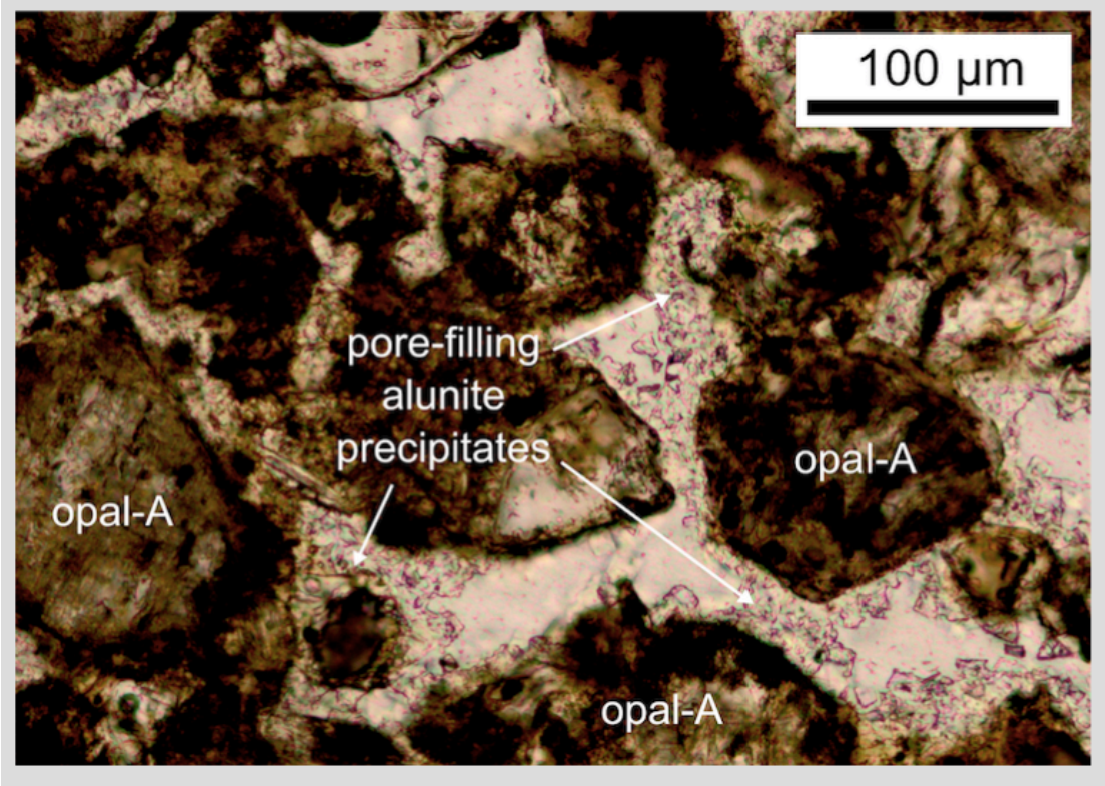

Figure 5. Optical microscope image showing pore-filling alunite precipitates in a sample of ash tuff (WI21). Image taken from *Heap et al.* (2015a).

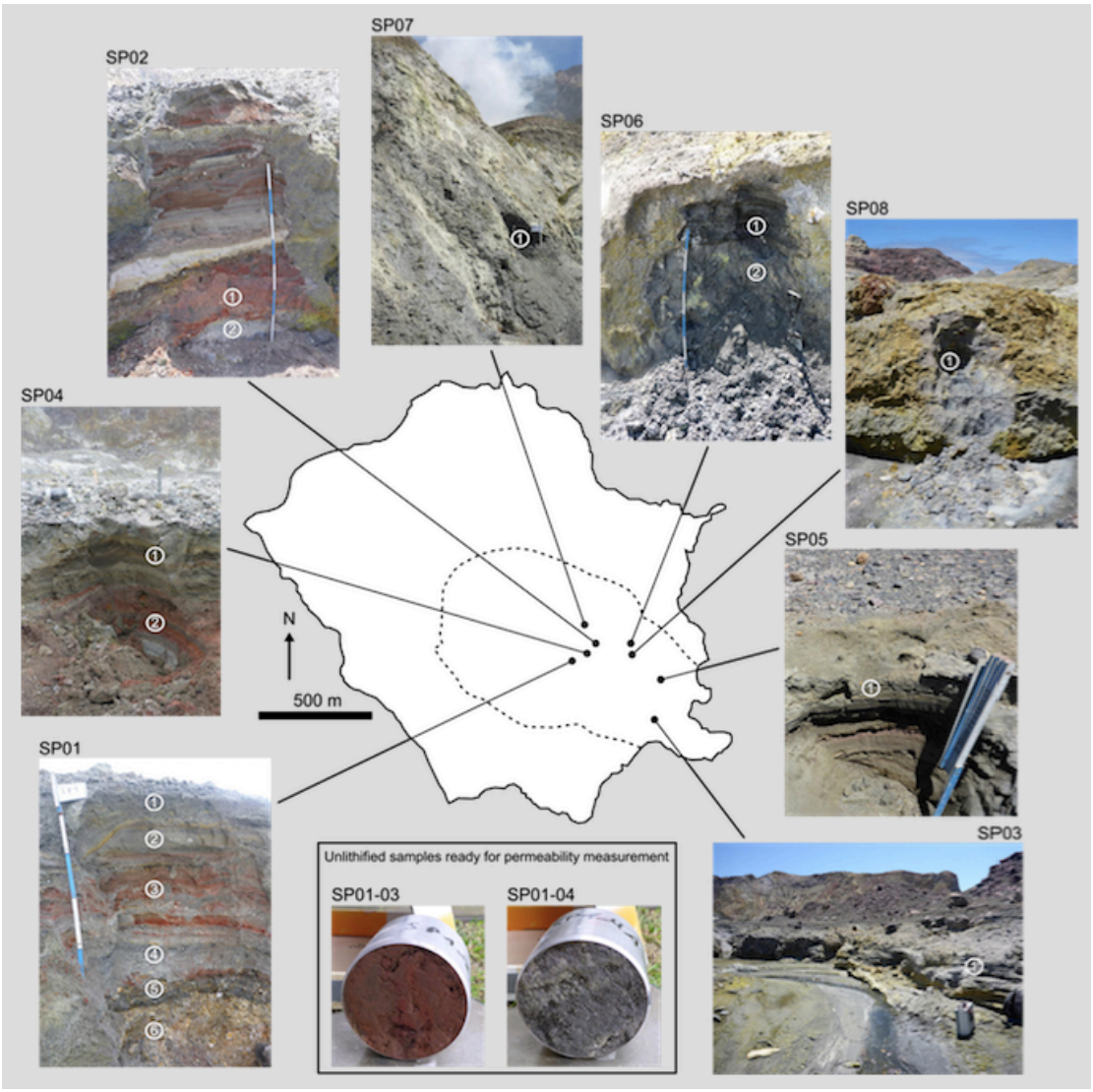

1135

1136 **Figure 6**. Locality and photographs of each of the eight trenches dug for unlithified

1137 material analysis (permeability, porosity, water content, and temperature). Numbers on

1138 the pictures indicate the sample number (Table A3). Inset shows two examples taken

1139 from trench SP01.

1140

1141

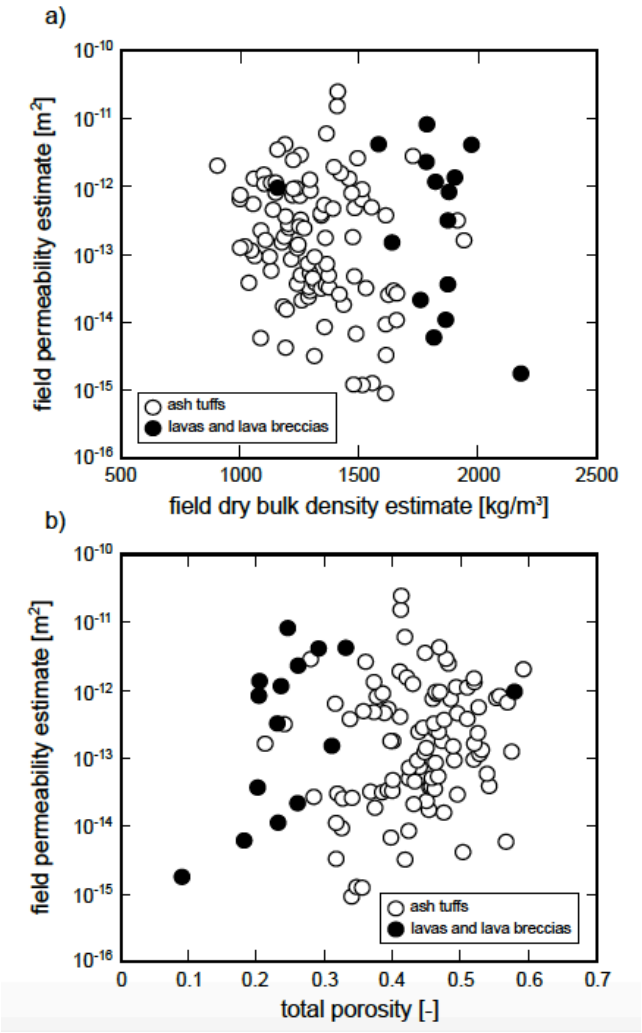

1142

1143 **Figure 7**. Field measurements on the lithified hand-sized sample blocks collected. (a)
1144 Field permeability (using the TinyPerm II) as a function of field dry bulk density. (b)
1145 Field permeability (using the TinyPerm II) as a function of total porosity. Data are
1146 available in Tables A1 and A2.

1147

1148

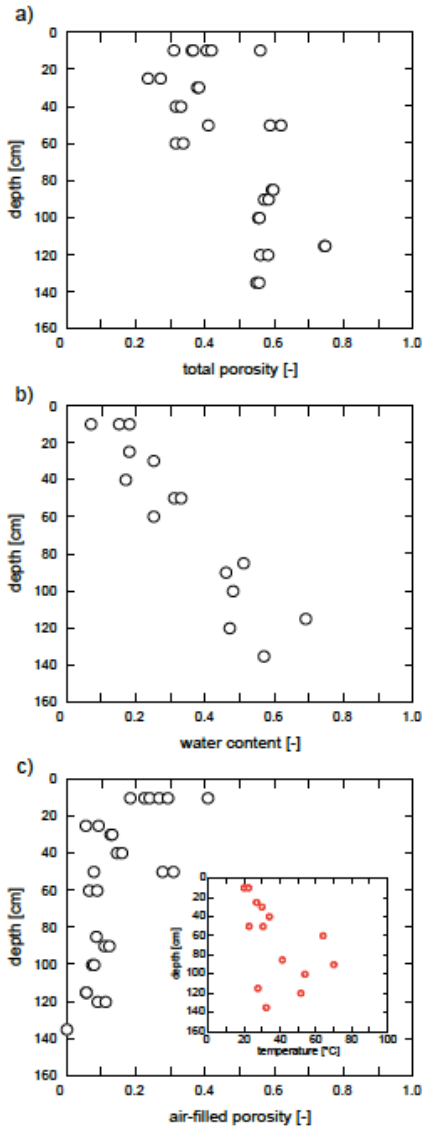

Figure 8. Field measurements on the unlithified materials from the eight trenches shown in Figure 6. (a) Depth as a function of total porosity. (b) Depth as a function of water content. (c) Depth as a function of air-filled porosity. Inset shows a graph of depth as a function of deposit temperature. Data are available in Table A3.

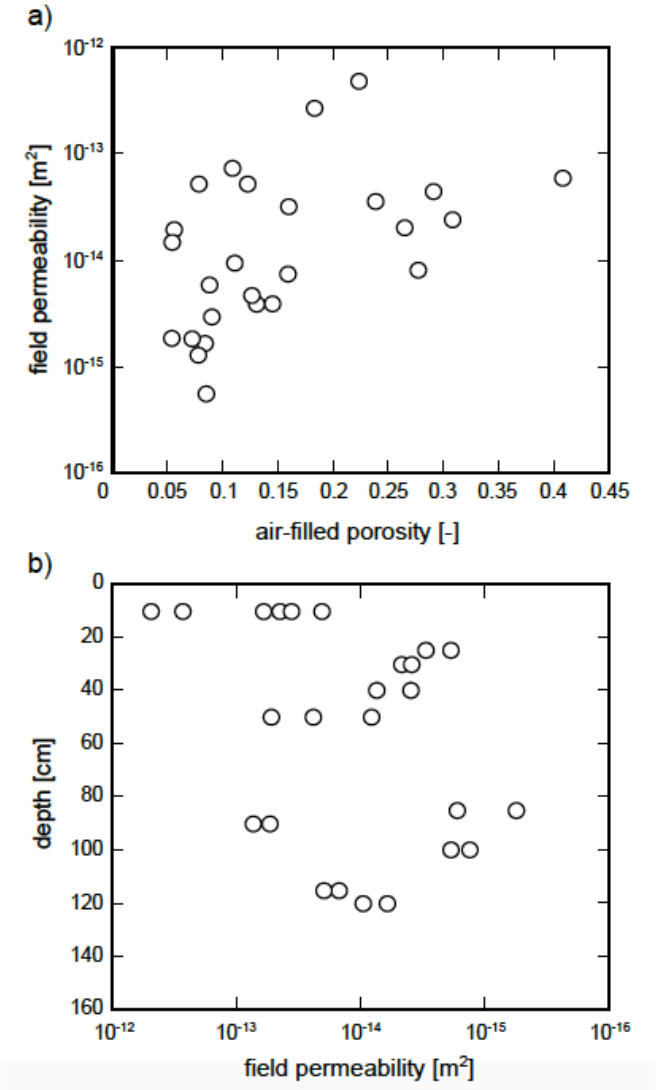

1156

1157 **Figure 9**. Field measurements on the unlithified materials from the eight trenches

1158 shown in Figure 6. (a) Field permeability as a function of air-filled porosity. (b) Depth as

1159 a function of field permeability. Data are available in Table A3.

1160

1161

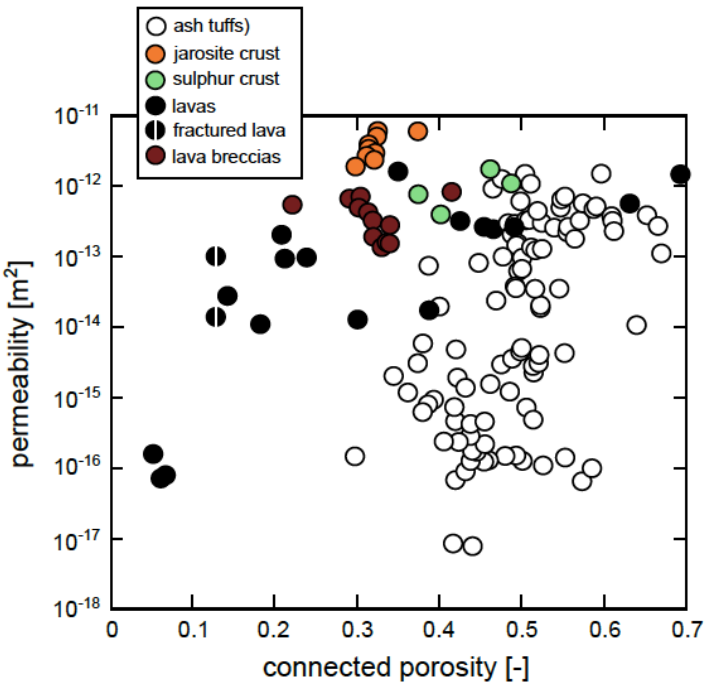

Figure 10. Laboratory measurements of permeability as a function of connected porosity for all of the 20 mm-diameter cylindrical samples of this study, plotted on log-linear axes. Data are available in Tables A4, A5, and A6. (For interpretation of the references to colour in this figure, the reader is referred to the web version of this article.)

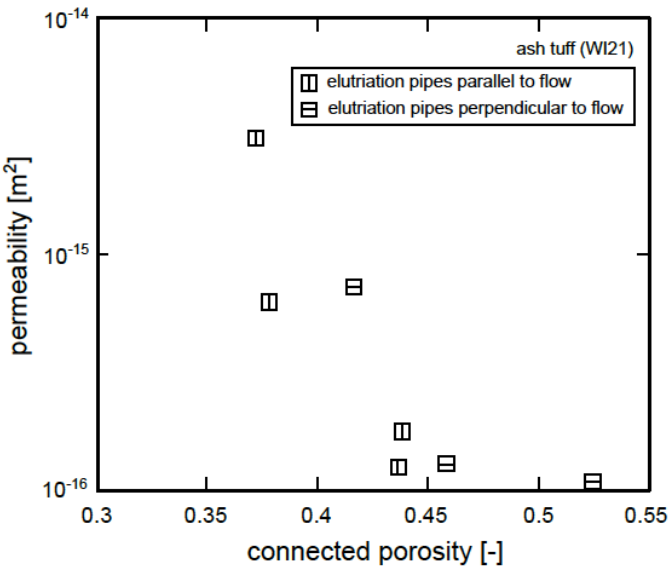

1170

1171 **Figure 11**. The influence of gas elutriation pipes on the permeability of ash tuff (WI21).

1172 Graph is a plot of permeability (measured in the laboratory; data available in Table A5)

1173 as a function of connected porosity.

1174

1175

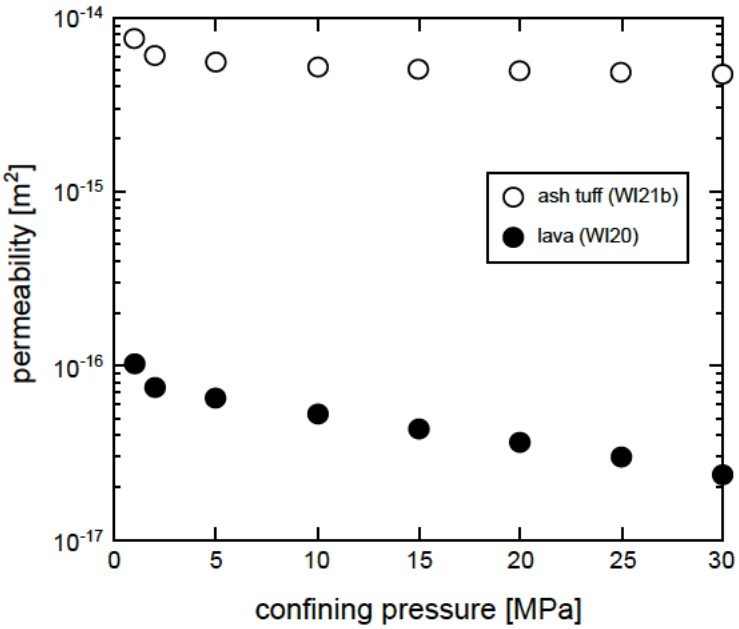

1176

1177 **Figure 12**. The influence of confining pressure (depth) on the permeability of lava

1178 (WI20) and ash tuff (WI21). Graph is a plot of permeability (measured in the laboratory;

1179 Table 4) as a function of confining pressure. Data are available in Table A7.

1180

1181

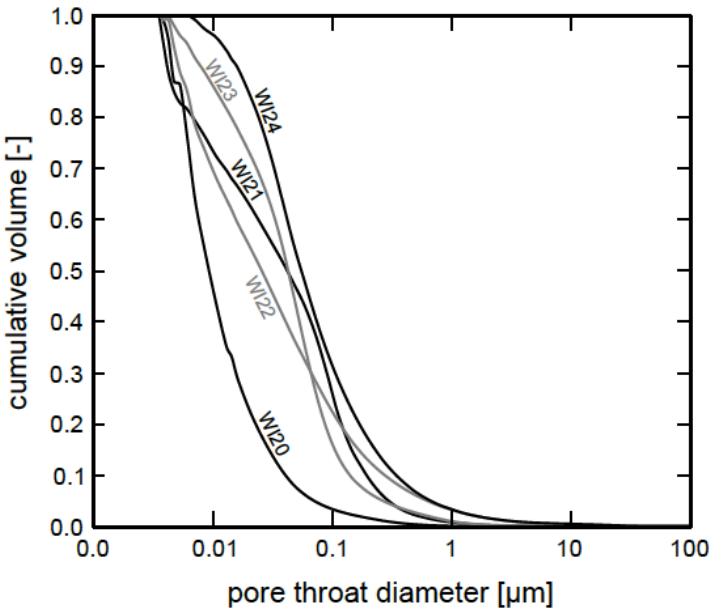

1182

1183 **Figure 13**. The distribution of pore throat diameters for WI20, WI21, WI22, WI23, and

1184 WI23 determined through mercury injection tests.

1185

1186

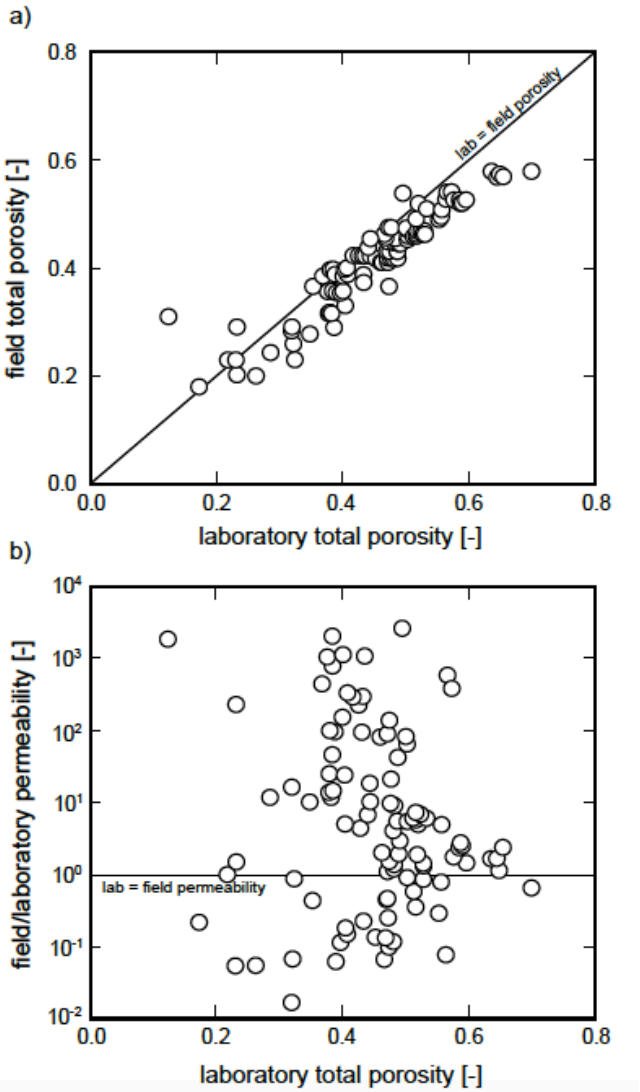

1187

1188 **Figure 14**. Laboratory versus field measurements of porosity and permeability. (a) Field

1189 total porosity as a function of laboratory total porosity. (b) The ratio of field to

1190 laboratory permeability as a function of laboratory total porosity.

1191

1192

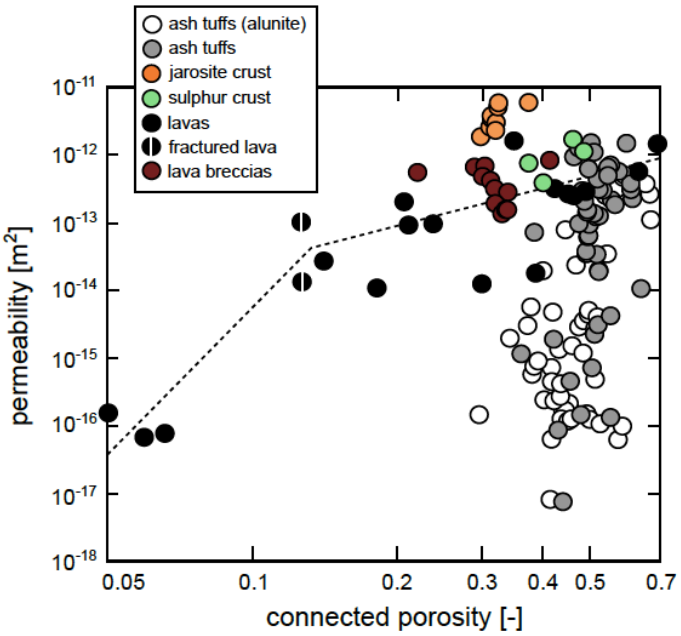

1193

1194 **Figure 15**. Laboratory measurements of permeability as a function of connected
1195 porosity for all of the 20 mm-diameter cylindrical samples of this study, plotted on log-
1196 log axes. The dashed lines indicate the two best-fit power law curves through the data,
1197 as determined using modified Bayesian Information Criterion (BIC) analysis (see text for
1198 details). Data are available in Tables A4, A5, and A6. (For interpretation of the
1199 references to colour in this figure, the reader is referred to the web version of this
1200 article.)

1201

1202

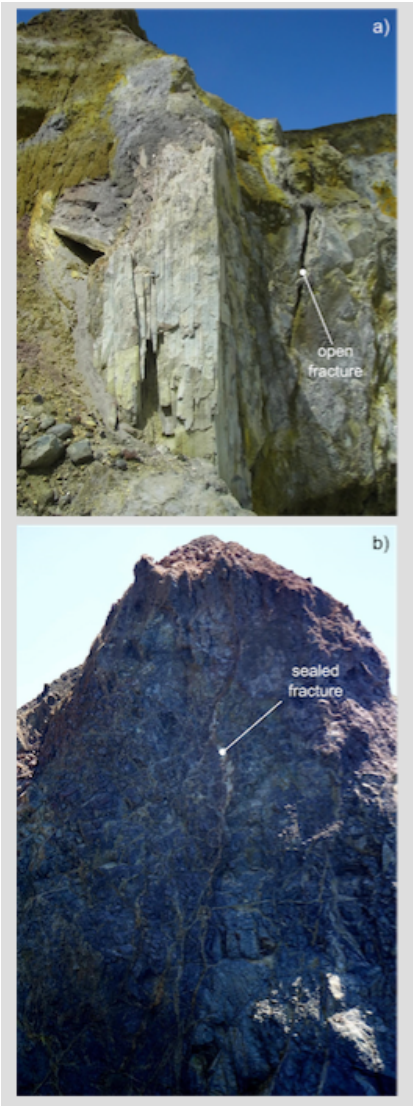

Figure 16. Macroscopic fractures in lavas at Whakaari. (a) Open fractures near the crater rim act as pathways for the subvertical flow of hydrothermal fluids. (b) Examples of sealed fractures that significantly reduce the permeability of the lava.

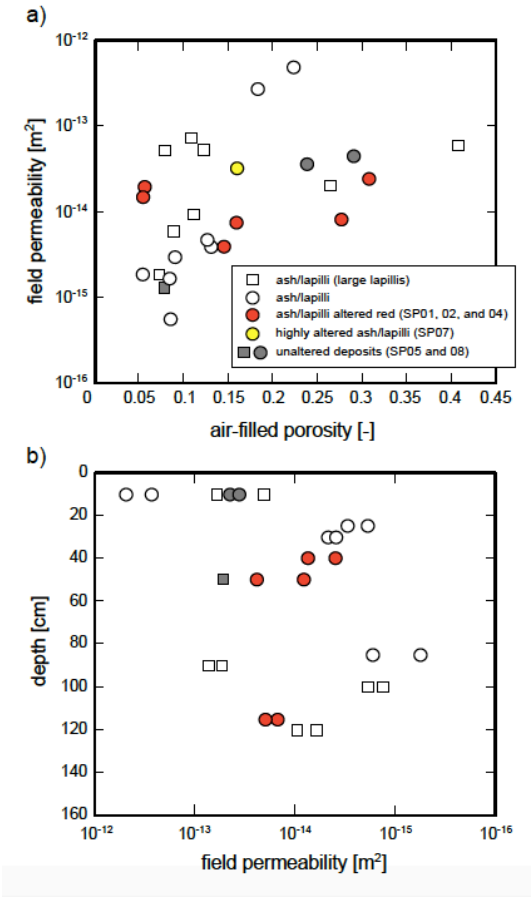

Figure 17. Field measurements on the unlithified materials from the eight trenches shown in Figure 6. (a) Field permeability as a function of air-filled porosity. (b) Depth as a function of field permeability. Graphs have been modified from Figure 9 to show textural features (lapilli or no lapilli) and alteration intensity. Data are available in Table A3.

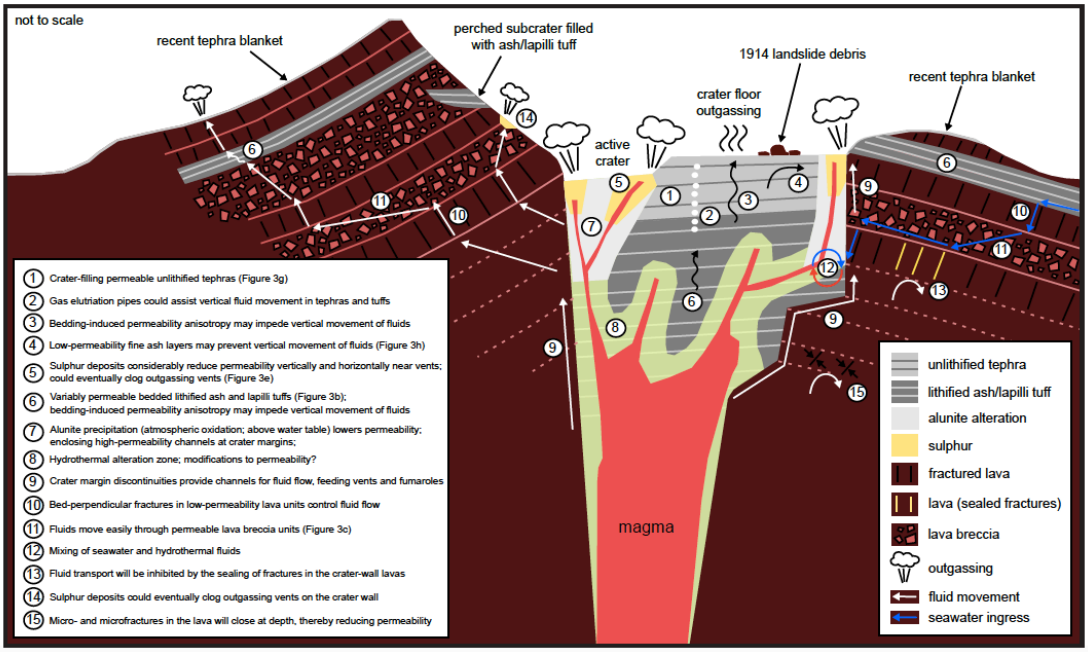

1217

1218 **Figure 18**. Cartoon cross section of Whakaari from west-northwest to east-southeast

1219 (not to scale) that captures the salient features of our study. See text for details.

1220

References

Ball, J.L., Stauffer, P.H., Calder, E.S., and Valentine, G.A. (2015), The hydrothermal alteration of cooling lava domes, *Bulletin of Volcanology*, 77:102.

Barberi, F., Bertangnini, A., Landi, P., and Principe, C. (1992), A review on phreatic eruptions and their precursors, *Journal of Volcanology and Geothermal Research*, *52*, 231-246.

Bean, C.J., De Barros, L., Lokmer, I., Métaxian, J.-P., O'Brien, G., and Murphy, S. (2014), Long-period seismicity in the shallow volcanic edifice formed from slow-rupture earthquakes, *Nature Geoscience*, *7*, 71-75.

Bergmann, J., Friedel, P., and Kleeberg, R. (1998), BGMN—A new fundamental parameters based Rietveld program for laboratory X-ray sources, its use in quantitative analysis and structure investigations, *CPD Newsletter*, *20*, 5-8.

Bertangnini, A., Landi, P., Santacroce, R., and Sbrana, A. (1991), The 1906 eruption of Vesuvius: from magmatic to phreatomagmatic activity through the flashing of a shallow depth hydrothermal system, *Bulletin of Volcanology*, *53*, 517-532.

Bibby, H.M., Caldwell, T.G., Davey, F.J., and Webb, T.H. (1995), Geophysical evidence on the structure of the Taupo Volcanic Zone and its hydrothermal circulation, *Journal of Volcanology and Geothermal Research*, *68*, 29-58.

Bloomberg, S., Werner, C., Rissmann, C., Mazot, A., Horton, T., Gravely, D., Kennedy, B.M., and Oze, C. (2014), Soil CO2 emissions as a proxy for heat and mass flow assessment, Taupo Volcanic Zone, New Zealand, *Geochemistry Geophysics Geosystems*, *15*, 4885-4904.

Bourbié, T., and Zinszner, B. (1985), Hydraulic and Acoustic Properties as a Function of Porosity in Fontainebleau Sandstone *Journal of Geophysical Research*, *90*, 11524-11532.

Brace, W.F., Walsh, J.B., and Frangos, W.T. (1968), Permeability of Granite under High Pressure, *Journal of Geophysical Research*, *73*, 2225-2236.

Brace, W.F. (1984), Permeability of crystalline rocks: New in situ measurements, *Journal of Geophysical Research*, *89*, 4327-4330.

Browne, P.R.L. (1978), Hydrothermal alteration in active geothermal fields, *Annual Reviews in Earth and Planetary Sciences*, *6*, 229-250.

BS5930 (1999), Code of Practice for Site Investigations, *British Standards Institution*, London.

Chardot, L., Jolly, A.D., Kennedy, B.M., Fournier, N., and Sherburn, S. (2015), Using volcanic tremor for eruption forecasting at White Island volcano (Whakaari), New Zealand, *Journal of Volcanology and Geothermal Research*, *302*, 11-23.

Christenson, B.W. (2000), Geochemistry of fluids associated with the 1995–1996 eruption of Mt. Ruapehu, New Zealand: signatures and processes in the magmatic-hydrothermal system, *Journal of Volcanology and Geothermal Research*, *97*, 1-30.

Christenson, B.W., Reyes, A.G., Young, R., Moebis, A., Sherburn, S., Cole-Baker, J., and Britten, K. (2010), Cyclic processes and factors leading to phreatic eruption events: Insights from the 25 September 2007 eruption through Ruapehu Crater Lake, New Zealand, *Journal of Volcanology and Geothermal Research*, *191*, 15-32.

Christenson, B.W., White, S., Britten, K., Scott, B.J., and Mazot, A. (2016), Hydrological evolution and chemical structure of a hyper-acidic spring-lake system on White Island, New Zealand. In review.

Clark, R.H., and Cole, J.W. (1986), White Island, *Late Cenozoic Volcanism in New Zealand*, *23*, 169-178.

Clauser, C. (1992), Permeability of crystalline rocks, *Earth and Space Science News*, *73*, 233-238.

Cole, J.W., Thordarson, T., and Burt, R.M. (2000), Magma Origin and Evolution of White Island (Whakaari) Volcano, Bay of Plenty, New Zealand, *Journal of Petrology*, *41(6)*, 867-895.

1275 Collinson, A.S.D., and Neuberg, J. (2012), Gas storage, transport and pressure changes in
1276 an evolving permeable volcanic edifice, *Journal of Volcanology and Geothermal*
1277 *Research*, *243-244*, 1-13.
1278 Collombet, M. (2009), Two-dimensional gas loss for silicic magma flows: toward more
1279 realistic numerical models, *Geophysical Journal International*, *177*, 309-318.
1280 Day, S.J. (1996), Hydrothermal pore fluid pressure and the stability of porous,
1281 permeable volcanoes, *Geological Society, London, Special Publications 110*, 77-93.
1282 Deino, A.L., Orsi, G., De Vita, S., and Piochi, M. (2004), The age of the Neapolitan Yellow
1283 Tuff caldera-forming eruption (Campi Flegrei caldera - Italy) assessed by
1284 40Ar/39Ar dating method, *Journal of Volcanology and Geothermal Research*, *133*,
1285 157-170.
1286 Donachie, S.P., Christenson, B.W., Kunkel, D.D., Malahoff, A., and Alam, M. (2002),
1287 Microbial community in acidic hydrothermal waters of volcanically active White
1288 Island, New Zealand, *Extremophiles*, 6, 419-425.
1289 del Potro, R., and Hürlimann, M. (2009), The decrease in the shear strength of volcanic
1290 materials with argillic hydrothermal alteration, insights from the summit region of
1291 Teide stratovolcano, Tenerife, *Engineering Geology*, *104*, 135-143.
1292 Ece, Ö., I., Schroeder, P.A., Smilley, M.J., and Wampler, J.M. (2008), Acid-sulphate
1293 hydrothermal alteration of andesitic tuffs and genesis of halloysite and alunite
1294 deposits in the Biga Peninsula, Turkey, *Clay Minerals*, *43*, 281-315.
1295 Edmonds, M., Oppenheimer, C., Pyle, D.M., Herd, R.A., and Thompson, G. (2003), SO2
1296 emissions from Soufrière Hills Volcano and their relationship to conduit
1297 permeability, hydrothermal interaction and degassing regime, *Journal of*
1298 *Volcanology and Geothermal Research*, *124*, 23-43.
1299 Eichelberger, J.C., Carrigan, C.R., Westrich, H.R., and Price, P.H. (1986), Non-explosive
1300 silicic volcanism, *Nature*, *323*, 598-602.
1301 Farquharson, J.I., Heap, M.J., Varley, N., Baud, P., and Reuschlé, T. (2015), Permeability
1302 and porosity relationships of edifice-forming andesites: A combined field and
1303 laboratory study, *Journal of Volcanology and Geothermal Research*, *297*, 52-68.
1304 Farquharson, J.I., Heap, M.J., Lavallée, Y., and Baud, P. (2016), Evidence for the
1305 development of permeability anisotropy in lava domes and volcanic conduits,
1306 *Journal of Volcanology and Geothermal Research*, *323*, 163-185.
1307 Faulkner, D.R., and Rutter, E. (2000), Comparisons of water and argon permeability in
1308 natural clay-bearing fault gouge under high pressure at 20°C, *Journal of*
1309 *Geophysical Research*, *105 (B7)*, 16415-16426.
1310 Fournier, N., and Chardot, L. (2012), Understanding volcano hydrothermal unrest from
1311 geodetic observations: Insights from numerical modeling and application to White
1312 Island volcano, New Zealand, *Journal of Geophysical Research*, *117*, B11, DOI:
1313 10.1029/2012JB009469.
1314 Frolova, J., Ladygin, V., Rychagov, S., and Zukhubaya, D. (2014), Effects of hydrothermal
1315 alterations on physical and mechanical properties of rocks in the Kuril–
1316 Kamchatka island arc, *Engineering Geology*, *183*, 80-95.
1317 Giggenbach, W.F., Shinohara, H., Kusakabe, M., and Ohba, T. (2003), Formation of acid
1318 volcanic brines through interaction of magmatic gases, seawater, and rock within
1319 the White Island volcanic-hydrothermal system, New Zealand, *Spec. Publ. Soc.*
1320 *Econ. Geol.*, *10*, 19-40.
1321 Griffiths, L., Heap, M.J., Wang, F., Daval, D., Gilg, H.A., Baud, P., Schmittbuhl, J., and Genter,
1322 A. (2016), Geothermal implications for fracture-filling hydrothermal precipitation,
1323 *Geothermics*, DOI: 10.1016/j.geothermics.2016.06.006.
1324 Harris, A.J.L., and Maciejewski, A.J.H. (2000), Thermal surveys of the Vulcano Fossa
1325 fumarole field 1994–1999: evidence for fumarole migration and sealing, *Journal of*
1326 *Volcanology and Geothermal Research*, *102*, 119-147.
1327 Heap, M.J., Lavallée, Y., Petrakova, L., Baud, P., Reuschlé, T., Varley, N., and Dingwell, D.B.
1328 (2014), Microstructural controls on the physical and mechanical properties of

edifice-forming andesites at Volcán de Colima, Mexico, *Journal of Geophysical Research*, *119*, 2925-2963.

Heap, M.J., Kennedy, B.M., Pernin, N., Jacquemard, L., Baud, P., Farquharson, I.J., Scheu, B., Lavallée, Y., Gilg, H.A., Letham-Brake, M., Mayer, K., Jolly, A.D., Reuschlé, T., and Dingwell, D.B. (2015a), Mechanical behaviour and failure modes in the Whakaari (White Island volcano) hydrothermal system, New Zealand, *Journal of Volcanology and Geothermal Research*, *295*, 26-42.

Heap, M.J., Farquharson, I.J., Wadsworth, F.B., Kolzenburg, S., and Russell, J.K. (2015b), Timescales for permeability reduction and strength recovery in densifying magma, *Earth and Planetary Science Letters*, *429*, 223-233.

Heap, M.J., and Kennedy, B.M. (2016), Exploring the scale-dependent permeability of fractured andesite, *Earth and Planetary Science Letters*, *447*, 139-150.

Heap, M.J., and Wadsworth, F.B. (2016), Closing an open system: Pore pressure changes in permeable edifice rock at high strain rates, *Journal of Volcanology and Geothermal Research*, *315*, 40-50.

Hedenquist, J.W., Simmons, S.F., Giggenbach, W.F., and Eldridge, C.S. (1993), White Island, New Zealand, volcanic-hydrothermal system represents the geochemical environment of high-sulfidation Cu and Au ore deposition, *Geology*, 21, 731-734.

Houghton, B.F., and Nairn, I.A. (1991), The 1976–1982 Strombolian and phreatomagmatic eruptions of White Island, New Zealand: eruptive and depositional mechanisms at a 'wet' volcano, *Bulletin of Volcanology*, *54*, 25-49.

Hurwitz, S., Christiansen, L.B., and Hsieh, P.A. (2007), Hydrothermal fluid flow and deformation in large calderas: Inferences from numerical simulations, *Journal of Geophysical Research*, *112*, B02206, doi:10.1029/2006JB004689.

Inoue, A. (1995) Formation of clay minerals in hydrothermal environments. In: Velde, B. (Ed.), Origin and Mineralogy of Clays. Springer, Berlin, pp. 268-329.

Jaupart, C. (1998), Gas loss from magmas through conduit walls during eruption, *Geological Society, London, Special Publications*, *145*, 73-90.

Johnston, J.H. (1977), Jarosite and akaganéite from White Island volcano, New Zealand: An X-ray and Mössbauer study, *Geochimica et Cosmochimica Acta*, *41*, 539-544.

Jolly, A., Kennedy, B.M., Edwards, M., Jousset, P., and Scheu, B. (2016), Infrasound tremor from bubble burst eruptions in the viscous shallow crater lake of White Island, New Zealand, and its implications for interpreting volcanic source processes, Journal of Volcanology and Geothermal Research, DOI: 10.1016/j.jvolgeores.2016.08.010.

Kaneshima, S., Kawakatsu, H., Matsubayashi, H., Sudo, Y., Tsutsui, T., Ohminato, T., Ito, H., Uhira, K., Yamasato, H., Oikawa, J., Takeo, M., and Iidaka, T. (1996), Mechanism of phreatic eruptions at Aso volcano inferred from near-field broadband seismic observations, *Science*, *273*, 642.

Kawada, Y., and Yoshida, S. (2010), Formation of a hydrothermal reservoir due to anhydrite precipitation in an arc volcano hydrothermal system, *Journal of Geophysical Research*, 115 (B11106), DOI: 10.1029/2010JB007708.

Kendrick, J.E., Lavallée, Y., Varley, N., Wadsworth, F.B., Lamb, O.D., and Vasseur, J. (2016), Blowing Off Steam: Tuffisite Formation As a Regulator for Lava Dome Eruptions, *Front. Earth Sci.*, doi: 10.3389/feart.2016.00041.

Kennedy, B., Wadsworth, F.B., Vasseur, J., Schipper, C.I., Jellinek, A.M., von Aulock, F.W., Hess, K.-U., Russell, J.K., Lavallée, Y., Nichols, A.R.L., and Dingwell, D.B. (2015), Surface tension driven processes densify and retain permeability in magma and lava, *Earth and Planetary Science Letters*, *433*, 116-124.

Klinkenberg, L.J. (1941), The permeability of porous media to liquids and gases, *Drilling and production practice*, 200-213.

Klug, C., and Cashman, K.V. (1996), Permeability development in vesiculating magmas: implications for fragmentation, *Bulletin of Volcanology*, *58*, 87-100.

Kueppers, U., Scheu, B., Spieler, O., and Dingwell, D.B. (2005), Field-based density measurements as tool to identify preeruption dome structure: set-up and first results from Unzen volcano, Japan, *Journal of Volcanology and Geothermal Research*, *141*, 65-75.

Kushnir, A.R.L., Martel, C., Bourdier, J.-L., Heap, M.J., Reuschlé, T., Erdmann, S., Komorowski, J.C., and Cholik, N. (2016), Probing permeability and microtexture: Unravelling the role of a low-permeability dome on the explosivity of Merapi (Indonesia), *Journal of Volcanology and Geothermal Research*, *316*, 56-71.

Leet, R.C. (1988), Saturated and subcooled hydrothermal boiling in groundwater flow channels as a source of harmonic tremor, *Journal of Geophysical Research*, *93*, 4835-4849.

Main, I.G., Leonard, T., Papasouliotis, O., Hatton, C.G., and Meredith, P.G. (1999), One slope or two? Detecting statistically significant breaks of slope in geophysical data, with application to fracture scaling relationships, *Geophysical Research Letters*, *26*, 2801-2804.

Mayer, K., Scheu, B., Gilg, H.A., Heap, M.J., Kennedy, B.M., Lavallée, Y., Letham-Brake, M., and Dingwell, D.B. (2015), Experimental constraints on phreatic eruption processes at Whakaari (White Island volcano), *Journal of Volcanology and Geothermal Research*, *302*, 150-162.

Mayer, K., Scheu, B., Montanaro, C., Yilmaz, T.I., Isaia, R., Aßbichler, D., and Dingwell, D.B. (2016a), Hydrothermal alteration of surficial rocks at Solfatara (Campi Flegrei): Petrophysical properties and implications for phreatic eruption processes, *Journal of Volcanology and Geothermal Research*, *320*, 128-143.

Mayer, K., Scheu, B., Rott, S., Montanaro, C., Yilmaz, T.I., Gilg, H.A., Joseph, E.P., and Dingwell, D.B. (2016b), Phreatic activity and hydrothermal alteration in the Valley of Desolation, Dominica, *Bulletin of Volcanology*, in review.

Mongillo, M.A., and Wood, C.P. (1995), Thermal infrared mapping of White Island volcano, New Zealand, *Journal of Volcanology and Geothermal Research*, *69*, 59-71.

Montanaro, C., Scheu, B., Gudmundsson, M.T., Vogfjörd, K., Reynolds, H.I., Dürig, T., Strehlow, K., Rott, S., Reuschlé, T., and Dingwell, D.B. (2016), Multidisciplinary constraints of hydrothermal explosions based on the 2013 Gengissig lake events, Kverkfjöll volcano, Iceland, *Earth and Planetary Science Letters*, *434*, 308-319.

Moon, V., Bradshaw, J., and de Lange, W. (2009), Geomorphic development of White Island Volcano based on slope stability modelling, *Engineering Geology*, *104*, 16-30.

Mueller, S., Melnik, O., Spieler, O., Scheu, B., and Dingwell, D.B. (2005), Permeability and degassing of dome lavas undergoing rapid decompression: an experimental study, *Bulletin of Volcanology*, *67*, 526-538.

Mutlu, H., Sariiz, K., and Kadir, S. (2005), Geochemistry and origin of the Şaphane alunite deposit, Western Anatolia, Turkey, *Ore Geology Reviews*, *26*, 39-50.

Nara, Y., Meredith, P.G., Yoneda, T., and Kaneko, K. (2011), Influence of macro-fractures and micro-fractures on permeability and elastic wave velocities in basalt at elevated pressure, *Tectonophysics*, *503*, 52-59.

Neuman, S.P. (1994), Generalized scaling of permeabilities: Validation and effect of support scale, *Geophysical Research Letters*, *21*, 349-352.

Nishi, Y., Sherburn, S., Scott, B.J., and Sugihara, M. (1996), High-frequency earthquakes at White Island volcano, New Zealand: insights into the shallow structure of a volcano-hydrothermal system, *Journal of Volcanology and Geothermal Research*, *72*, 183-197.

Peiffer, L., Bernard-Romero, R., Mazot, A., Taran, Y.A., Guevara, M., and Santoyo, E. (2014), Fluid geochemistry and soil gas fluxes (CO2-CH4-H2S) at a promissory Hot Dry Rock Geothermal System : the Acoculco caldera, Mexico., *Journal of Volcanology and Geothermal Research*, *284*, 122-137.

1435 Peltier, A., Scott, B.J., and Hurst, T. (2009), Ground deformation patterns at White Island
1436 volcano (New Zealand) between 1967 and 2008 deduced from levelling data,
1437 *Journal of Volcanology and Geothermal Research*, *181*, 207-218.
1438 Pirajno, F. (2009), Hydrothermal Processes and Mineral Systems. Springer, Netherlands,
1439 p. 1250.
1440 Pola, A., Crosta, G.B., Fusi, N., Barberini, V., and Norini, G. (2012), Influence of alteration
1441 on physical properties of volcanic rocks, *Tectonophysics*, *566-567*, 67-86.
1442 Pola, A., Crosta, G.B., Fusi, N., and Castellanza, R. (2014), General characterization of the
1443 mechanical behaviour of different volcanic rocks with respect to alteration,
1444 *Engineering Geology*, *169*, 1-13.
1445 Procter, J.N., Cronin, S.J., Zernack, A.V., Lube, G., Stewart, R.B., Nemeth, K., and Keys, H.
1446 (2014), Debris flow evolution and the activation of an explosive hydrothermal
1447 system; Te Maari, Tongariro, New Zealand, *Journal of Volcanology and Geothermal*
1448 *Research*, *286*, 331-347.
1449 Reed, M. H., (1997), Hydrothermal alteration and its relationship to ore fluid
1450 composition. In: Barnel H.L. (Ed.), Geochemistry of hydrothermal ore deposits. 3rd
1451 Ed. Wiley, New York, pp 303-366.
1452 Reid, M.E., Sisson, T.W., and Brien, D.L. (2001), Volcano collapse promoted by
1453 hydrothermal alteration and edifice shape, Mount Rainier, Washington, *Geology*,
1454 *29*, 779-782.
1455 Reid, M.E. (2004), Massive collapse of volcano edifices triggered by hydrothermal
1456 pressurization, *Geology*, *32*, 373-376.
1457 Rowland, J.V., and Sibson, R.H. (2004), Structural controls on hydrothermal flow in a
1458 segmented rift system, Taupo Volcanic Zone, New Zealand, *Geofluids*, *4*, 259-283.
1459 Rust, A., and Cashman, K.V. (2004), Permeability of vesicular silicic magma: inertial and
1460 hysteresis effects, *Earth and Planetary Science Letters*, *228*, 93-107.
1461 Rye R.O., Bethke P.M., Wasserman M.D. (2002), The stable isotope geochemeistry of acid
1462 sulfate alteration, *Economic Geology, 87*, 225-262.
1463 Saar, M.O., and Manga, M. (1999), Permeability-porosity relationship in vesicular basalts,
1464 *Geophysical Research Letters*, *26*, 111-114.
1465 Schaefer, L.N., Kendrick, J.E., Oommen, T., Lavallée, Y., and Chigna, G. (2015),
1466 Geomechanical rock properties of a basaltic volcano, *Front. Earth Sci.*, *3*, 29, doi:
1467 10.3389/feart.2015.00029.
1468 Selvadurai, A.P.S., and Selvadurai, P.A. (2010), Surface permeability tests: experiments
1469 and modelling for estimating effective permeability, *Proceedings of the Royal*
1470 *Society A*, *466*, DOI: 10.1098/rspa.2009.0475.
1471 Sherburn, S., Scott, B.J., Nishi, Y., and Sugihara, M. (1998), Seismicity at White Island
1472 volcano, New Zealand: a revised classification and inferences about source
1473 mechanism, *Journal of Volcanology and Geothermal Research*, *83*, 287-312.
1474 Siratovich, P., Heap, M.J., Villeneuve, M.C., Cole, J.W., and Reuschlé, T. (2014), Physical
1475 property relationships of the Rotokawa Andesite, a significant geothermal
1476 reservoir rock in the Taupo Volcanic Zone, New Zealand, *Geothermal Energy*, *2:10*,
1477 doi:10.1186/s40517-014-0010-4.
1478 Steiner, A. (1968), Clay minerals in hydrothermally altered rocks at Wairakei, New
1479 Zealand, *Clays and Clay Minerals*, *16*, 193-213.
1480 Tanikawa, W., and Shimamoto, T. (2009), Comparison of Klinkenberg-corrected gas
1481 permeability and water permeability in sedimentary rocks, *International Journal*
1482 *of Rock Mechanics and Mining Sciences*, *46*, 229-238.
1483 Todesco, M., Rinaldi, A.P., and Bonforte, A. (2010), Modeling of unrest signals in
1484 heterogeneous hydrothermal systems, *Journal of Geophysical Research*, *115*,
1485 B09213, doi: 10.1029/2010JB007474.
1486 Vinciguerra, S., Trovato, C., Meredith, P.G., and Benson, P.M. (2005), Relating seismic
1487 velocities, thermal cracking and permeability in Mt. Etna and Iceland basalts,
1488 *International Journal of Rock Mechanics and Mining Sciences*, *42*, 900-910.

1489 Voight, B., and Elsworth, D. (1997), Failure of volcano slopes, *Geotechnique*, *47*, 1-31.
1490 Wadsworth, F.B., Vasseur, J., Scheu, B., Kendrick, J.E., Lavallée, Y., and Dingwell, D.B.
1491 (2016), Universal scaling of fluid permeability during volcanic welding and
1492 sediment diagenesis, *Geology*, *44*, 219-222.
1493 Werner, C., Hurst, T., Scott, B.J., Sherburn, S., Christensen, B.W., Britten, K., Cole-Baker, J.,
1494 and Mullan, B. (2008), Variability of passive gas emissions, seismicity, and
1495 deformation during crater lake growth at White Island Volcano, New Zealand,
1496 2002–2006, *Journal of Geophysical Research*, *113*, B1, DOI:
1497 10.1029/2007JB005094.
1498 Wright, H.M.N., Cashman, K.V., Gottesfeld, E.H., and Roberts, J.J. (2009), Pore structure of
1499 volcanic clasts: Measurements of permeability and electrical conductivity, *Earth*
1500 *and Planetary Science Letters*, *280*, 93-104.
1501 Wyering, L.D., Villeneuve, M.C., Wallis, I.C., Siratovich, P., Kennedy, B., Gravely, D.M., and
1502 Cant, J.L. (2014), Mechanical and physical properties of hydrothermally altered
1503 rocks, Taupo Volcanic Zone, New Zealand, *Journal of Volcanology and Geothermal*
1504 *Research*, *288*, 76-93.
1505 Wyering, L.D., Villeneuve, M.C., Wallis, I.C., Siratovich, P., Kennedy, B.M., and Gravely, D.
1506 (2015), The development and application of the alteration strength index
1507 equation, *Engineering Geology*, *199*, 48-61.
1508 Zhu, W., and Wong, T.-f. (1997), The transition from brittle faulting to cataclastic flow:
1509 Permeability evolution, *Journal of Geophysical Research*, *102, No. B2*, 3027-3041.
1510 Zimbelman, D. R., Rye, R. O., and Breit, G. N. (2005), Origin of secondary sulfate minerals
1511 on active andesitic stratovolcanoes. *Chemical Geology*, 215(1), 37-60.

Appendix

The goal of our appendix is twofold. First, in the interests of transparency and future reinterpretation, we are keen to show photographs of each of the hand-sized lithified blocks collected (Figures A1-A5) and each of the 20 mm-diameter laboratory samples (Figures A6-A12). Second, we are keen to future studies to use our data. To this end, we offer all of the field and laboratory data in seven tables (Tables A1-A7).

Appendix figure captions

Figure A1. Photographs of the hand-sized sample lava and lava breccia blocks. Each square on the scale bar is 10 mm.

Figure A2. Photographs of the hand-sized sample lithified ash tuff blocks**.** Each square on the scale bar is 10 mm.

Figure A3. Photographs of the hand-sized sample lithified ash tuff blocks (continued)**.** Each square on the scale bar is 10 mm.

Figure A4. Photographs of the hand-sized sample lithified ash tuff blocks (continued)**.** Each square on the scale bar is 10 mm.

Figure A5. Photographs of the hand-sized sample lithified ash tuff blocks (continued)**.** Each square on the scale bar is 10 mm.

Figure A6. Photographs of the 20 mm-diameter lava and lava breccia laboratory samples. Missing samples: WI20_1 and WI20_B.

Figure A7. Photographs of the 20 mm-diameter lava and lava breccia laboratory samples (continued)**.**

Figure A8. Photographs of the 20 mm-diameter lithified ash tuff laboratory samples**.**

Figure A9. Photographs of the 20 mm-diameter lithified ash tuff laboratory samples (continued)**.**

Figure A10. Photographs of the 20 mm-diameter lithified ash tuff laboratory samples (continued)**.**

Figure A11. Photographs of the 20 mm-diameter lithified ash tuff laboratory samples (continued)**.**

Figure A12. Photographs of the 20 mm-diameter surficial laboratory samples (jarosite and sulphur crust, and sulphur flow)**.** Missing samples: WI25_A, WI25_G, WI26_B, and WI26_D.

1556 **Table A1**. Summary of the field data for the lava and lava breccia blocks. Photographs of

1557 the blocks are provided in Figures A1-A2.

1558

Sample	Bulk density (kg/m^3)	Skeletal density (kg/m^3)	Total porosity	TinyPerm permeability estimate (m^2)	Notes
WI-F-90	1478	2466	0.40	4.79×10^{-14}	
WI-F-91	1656	2313	0.28	2.73×10^{-14}	
WI-F-92	1724	2393	0.28	2.90×10^{-12}	
WI-F-96	1154	2745	0.58	9.65×10^{-13}	Vesicular
WI-F-97	1901	2391	0.20	1.36×10^{-12}	Red/brown surface discolouration
WI-F-98	1581	2363	0.33	4.24×10^{-12}	Vesicular
WI-F-99	1812	2214	0.18	6.09×10^{-15}	Red/yellow surface discolouration
WI-F-100	1821	2383	0.24	1.18×10^{-12}	
WI-F-101	1756	2376	0.26	2.16×10^{-14}	
WI-F-102	1874	2354	0.20	8.44×10^{-13}	
WI-F-103	1784	2364	0.25	8.31×10^{-12}	
WI-F-104	1872	2434	0.23	3.23×10^{-13}	
WI-F-105	1860	2421	0.23	1.11×10^{-14}	
WI-F-106	2178	2394	0.09	1.78×10^{-15}	
WI-F-107	1871	2344	0.20	3.65×10^{-14}	
WI-F-111	1316	2426	0.46	3.83×10^{-14}	Red/yellow surface discolouration
WI-F-114	1637	2375	0.31	1.50×10^{-13}	White/yellow surface discolouration
WI-F-116	1973	2784	0.29	4.11×10^{-12}	Red surface discolouration
WI-F-119	1781	2411	0.26	2.31×10^{-12}	Lava breccia

1559

1560 **Table A2**. Summary of the field data for the lithified ash tuff blocks. Photographs of the
1561 blocks are provided in Figures A2-A5. Bulk dry density could not be determined for
1562 those samples that floated; in this case, total porosity was calculated assuming a bulk
1563 dry density of 1000 kg/m^3 (values indicated with an asterisk).
1564

Sample	Bulk dry density (kg/m^3)	Skeletal density (kg/m^3)	Total porosity	TinyPerm permeability estimate (m^2)	Notes
WI-F-1	1351	2228	0.39	5.30×10^{-13}	Bedded
WI-F-2	1370	2379	0.42	5.00×10^{-14}	
WI-F-3	1033	2257	0.54	3.86×10^{-14}	
WI-F-4	1354	2348	0.42	8.57×10^{-15}	
WI-F-5	1086	2289	0.53	2.35×10^{-13}	
WI-F-6	1189	2395	0.50	4.23×10^{-15}	
WI-F-8	1416	2103	0.33	2.57×10^{-14}	Bedded
WI-F-9	1285	2338	0.45	2.53×10^{-14}	
WI-F-10	1016	2167	0.53	1.32×10^{-13}	
WI-F-11	1472	2443	0.40	1.79×10^{-13}	
WI-F-12	1219	2370	0.49	7.49×10^{-13}	
WI-F-13	1260	2213	0.43	2.10×10^{-14}	
WI-F-14	1182	2240	0.47	1.83×10^{-13}	Bedded
WI-F-15	1250	2397	0.48	2.94×10^{-12}	
WI-F-16	Floater	2212	0.55*	2.06×10^{-12}	
WI-F-17	1469	2358	0.38	8.08×10^{-13}	
WI-F-18	1433	2291	0.37	1.85×10^{-14}	Bedded
WI-F-19	1356	2259	0.40	1.70×10^{-13}	
WI-F-20	1247	2308	0.46	7.42×10^{-13}	
WI-F-21	1490	2330	0.36	2.61×10^{-12}	
WI-F-23	1099	2290	0.52	1.49×10^{-12}	
WI-F-24	1372	2260	0.39	3.30×10^{-14}	Bedded
WI-F-25	1052	2224	0.53	5.56×10^{-13}	
WI-F-26	1293	2428	0.47	5.26×10^{-14}	
WI-F-27	1390	2273	0.39	4.65×10^{-13}	
WI-F-28	1222	2363	0.48	2.45×10^{-12}	
WI-F-29	1295	2420	0.46	8.75×10^{-13}	
WI-F-30	1291	2264	0.43	1.25×10^{-12}	
WI-F-31	1061	2211	0.52	9.46×10^{-14}	
WI-F-32	1174	2298	0.49	1.50×10^{-13}	
WI-F-33	1313	2330	0.44	9.27×10^{-14}	
WI-F-34	1250	2329	0.46	2.58×10^{-13}	
WI-F-35	1304	2296	0.43	4.49×10^{-14}	
WI-F-36	1363	2368	0.42	7.23×10^{-14}	
WI-F-37	1475	2284	0.35	1.23×10^{-15}	
WI-F-38	1611	2431	0.34	3.72×10^{-13}	
WI-F-39	1253	2310	0.46	5.02×10^{-14}	
WI-F-40	1478	2359	0.37	4.78×10^{-13}	
WI-F-41	1623	2460	0.34	2.56×10^{-14}	
WI-F-42	1193	2274	0.48	1.57×10^{-14}	
WI-F-43	1146	2265	0.49	1.13×10^{-12}	
WI-F-44	1059	2206	0.52	1.30×10^{-12}	
WI-F-45	1456	2320	0.37	1.33×10^{-12}	

WI-F-46	Floater	2323	0.57*	6.51×10^{-13}	
WI-F-47	1239	2244	0.45	1.23×10^{-13}	Bedded
WI-F-48	1137	2254	0.50	4.57×10^{-13}	
WI-F-49	1338	2179	0.39	3.17×10^{-14}	Lapilli fragments
WI-F-50	1937	2460	0.21	1.65×10^{-13}	
WI-F-51	1285	2293	0.44	7.37×10^{-14}	
WI-F-52	1656	2424	0.32	1.10×10^{-14}	
WI-F-53	1106	2306	0.52	1.62×10^{-13}	
WI-F-54	1510	2458	0.39	9.04×10^{-13}	
WI-F-55	1392	2363	0.41	1.91×10^{-12}	
WI-F-56	1201	2166	0.45	2.83×10^{-13}	
WI-F-57	1611	2437	0.34	9.25×10^{-16}	Bedded
WI-F-58	1511	2343	0.35	1.23×10^{-15}	
WI-F-59	Floater	2353	0.58*	1.26×10^{-13}	
WI-F-60	1311	2256	0.42	3.24×10^{-15}	
WI-F-62	1154	2092	0.45	3.54×10^{-12}	
WI-F-63	1337	2271	0.14	4.08×10^{-13}	
WI-F-65	1213	2259	0.46	8.64×10^{-14}	Bedded
WI-F-66	1243	2256	0.45	1.39×10^{-13}	
WI-F-67	1222	2301	0.47	9.38×10^{-13}	
WI-F-68	1204	2263	0.47	2.46×10^{-13}	Bedded
WI-F-69	1360	2525	0.46	3.52×10^{-14}	
WI-F-70	1360	2339	0.42	6.15×10^{-12}	
WI-F-71	1236	2305	0.46	9.47×10^{-13}	
WI-F-72	1252	2324	0.46	3.23×10^{-13}	
WI-F-73	1269	2258	0.44	2.44×10^{-13}	Yellow surface discolouration
WI-F-74	1046	2216	0.53	1.15×10^{-13}	
WI-F-75	1643	2412	0.32	3.00×10^{-14}	
WI-F-76	1180	2159	0.45	1.73×10^{-14}	
WI-F-77	Floater	2237	0.55*	7.55×10^{-13}	Bedded
WI-F-78	1238	2272	0.46	3.72×10^{-14}	
WI-F-79	1123	2207	0.49	9.40×10^{-14}	
WI-F-80	1610	2385	0.32	9.28×10^{-15}	Lapilli fragments
WI-F-81	1187	2235	0.47	4.23×10^{-12}	
WI-F-82	1421	2453	0.42	1.55×10^{-12}	Lapilli fragments
WI-F-83	1131	2235	0.49	1.12×10^{-12}	
WI-F-84	1910	2515	0.24	3.17×10^{-13}	Red surface discolouration
WI-F-85	1612	2360	0.32	3.33×10^{-15}	
WI-F-86	1554	2381	0.35	1.28×10^{-15}	
WI-F-87	1406	2395	0.41	2.50×10^{-11}	Lapilli fragments
WI-F-88	1341	2738	0.51	3.77×10^{-13}	
WI-F-89	1407	2394	0.41	1.55×10^{-11}	Lapilli fragments
WI-F-93	1290	2147	0.40	3.30×10^{-14}	Bedded
WI-F-94	1511	2208	0.32	6.45×10^{-13}	Lapilli fragments
WI-F-95	1525	2410	0.37	3.21×10^{-14}	Sulphur
WI-F-108	1084	2503	0.57	5.90×10^{-15}	Sulphur
WI-F-109	1290	2555	0.49	2.93×10^{-14}	Sulphur
WI-F-110	1488	2471	0.40	6.85×10^{-15}	Red surface

					discolouration
WI-F-112	1549	2412	0.36	4.95×10^{-13}	Sulphur
WI-F-113	1129	2451	0.54	5.83×10^{-14}	Sulphur
WI-F-115	1190	2269	0.48	3.65×10^{-13}	Sulphur
WI-F-117	1149	2593	0.56	8.15×10^{-13}	Sulphur
WI-F-118	1100	2245	0.51	1.10×10^{-12}	

1565

1566

1567 **Table A3**. Summary of the field data for the unlithified deposits.

1568

Trench	Sample	Depth (cm)	Temperature (°C)	Dry bulk density (kg/m³)	Skeletal density (kg/m³)	Total porosity	Water saturation	Air-filled porosity	Field permeability estimate (m²)
SP01	01-A	10	22.4	1324	2220	0.40	0.18	0.22	4.88×10^{-13}
SP01	01-B	10	22.4	1414	2220	0.36	0.18	0.18	2.72×10^{-13}
SP01	02-A	30	30.0	1359	2180	0.38	0.25	0.13	4.69×10^{-15}
SP01	02-B	30	30.0	1350	2180	0.38	0.25	0.13	3.94×10^{-15}
SP01	03-A	50	30.5	867	2100	0.59	0.31	0.28	8.25×10^{-15}
SP01	03-B	50	30.5	803	2100	0.62	0.31	0.31	2.44×10^{-14}
SP01	04-A	85	41.3	791	1950	0.59	0.51	0.08	1.69×10^{-15}
SP01	04-A	85	41.3	789	1950	0.60	0.51	0.09	5.63×10^{-16}
SP01	05-A	100	54.0	894	2000	0.55	0.48	0.07	1.88×10^{-15}
SP01	05-B	100	54.0	884	2000	0.56	0.48	0.08	1.31×10^{-15}
SP01	06-A	120	51.7	826	1870	0.56	0.47	0.09	6.00×10^{-15}
SP01	06-B	120	51.7	783	1870	0.58	0.47	0.11	9.57×10^{-15}
SP02	01-A	115	27.8	528	2080	0.75	0.69	0.06	1.97×10^{-14}
SP02	01-B	115	27.8	532	2080	0.74	0.69	0.05	1.50×10^{-14}
SP02	02-A	135	32.2	746	1650	0.55	0.57	0.00	Out of range
SP02	02-B	135	32.2	734	1650	0.55	0.57	0.00	Out of range
SP03	01-A	10	20.0	1246	2130	0.41	0.15	0.26	2.06×10^{-14}
SP03	01-B	10	20.0	942	2130	0.56	0.15	0.41	6.00×10^{-14}
SP04	01-A	25	26.8	1255	1720	0.27	0.18	0.09	3.00×10^{-15}
SP04	01-B	25	26.8	1318	1720	0.23	0.18	0.05	1.88×10^{-15}
SP04	02-A	40	34.1	1080	1610	0.33	0.17	0.16	7.50×10^{-15}
SP04	02-B	40	34.1	1103	1610	0.31	0.17	0.14	1.88×10^{-15}
SP05	01-A	10	20.0	1375	2150	0.36	0.07	0.29	4.50×10^{-14}
SP05	01-B	10	20.0	1487	2150	0.31	0.07	0.24	3.62×10^{-15}
SP06	01-A	60	64.0	1145	1670	0.31	0.25	0.06	Out of range
SP06	01-B	60	64.0	1109	1670	0.34	0.25	0.09	Out of range
SP06	02-A	90	70.0	827	1980	0.58	0.46	0.12	5.35×10^{-14}
SP06	02-B	90	70.0	853	1980	0.57	0.46	0.11	7.35×10^{-14}
SP07	01	-	97.8	1091	1880	0.42	0.26	0.16	3.25×10^{-14}
SP08	01	50	22.8	1142	1930	0.41	0.33	0.08	5.25×10^{-14}

1569

1570 **Table A4**. Summary of the laboratory data for the 36 lava and lava breccia samples.
1571 Permeability (nitrogen) was measured under a confining pressure of 1 MPa unless
1572 otherwise stated. Photographs of the samples are provided in Figures A6 and A7.
1573 Fracture permeability k_f is provided for samples WI20_D and WI20_E using the
1574 approach outlined in *Heap and Kennedy* (2016) (see text for details).
1575

Sample	Dry bulk density (kg/m^3)	Connected porosity	Permeability (m^2)	Notes
WI20_1	2525	0.05	1.58×10^{-16}	Pc = 2 MPa
WI20_A	2542	0.06	7.05×10^{-17}	
WI20_B	2512	0.05	-	
WI20_C	2517	0.07	$< 10^{-18}$	
WI20_D	2382	0.13	1.38×10^{-14} ($k_f = 4.3 \times 10^{-13}$)	Macrocracks parallel to flow; Pc = 2 MPa
WI20_E	1419	0.13	1.04×10^{-13} ($k_f = 3.3 \times 10^{-12}$)	Macrocracks parallel to flow; Pc = 2 MPa
WI30_1	1564	0.33	1.57×10^{-13}	Breccia
WI30_2	1579	0.33	1.37×10^{-13}	Breccia
WI30_3	1658	0.30	4.93×10^{-13}	Breccia
WI30_4	1828	0.24	9.93×10^{-14}	Breccia
WI30_5	1551	0.34	1.56×10^{-13}	Breccia
WI30_6	1612	0.31	4.24×10^{-13}	Breccia
WI30_7	1929	0.21	9.38×10^{-14}	Breccia
WI30_8	1587	0.32	1.92×10^{-13}	Breccia
WI-F-90_1	1467	0.45	2.66×10^{-13}	
WI-F-90_2	1463	0.42	3.24×10^{-13}	
WI-F-91	1575	0.35	1.65×10^{-12}	
WI-F-92	1560	0.34	2.84×10^{-13}	
WI-F-96_1	1000	0.63	5.77×10^{-13}	Vesicular
WI-F-96_2	825	0.69	1.48×10^{-12}	Vesicular
WI-F-98	1409	0.41	8.37×10^{-13}	Breccia
WI-F-99	1831	0.14	2.79×10^{-14}	Pale discolouration
WI-F-101	1613	0.32	3.23×10^{-13}	Breccia
WI-F-102	1808	0.22	5.55×10^{-13}	Breccia
WI-F-103	1690	0.30	6.97×10^{-13}	Breccia
WI-F-105_1	1894	0.18	1.11×10^{-14}	
WI-F-105_2	1637	0.30	1.28×10^{-14}	
WI-F-105_3	1863	0.21	2.07×10^{-13}	
WI-F-106	2272	0.04	$< 10^{-18}$	Permeability too low for benchtop measurement
WI-F-107	1728	0.29	6.69×10^{-13}	
WI-F-111_1	1290	0.49	2.90×10^{-13}	
WI-F-111_2	1260	0.51	3.34×10^{-13}	
WI-F-114	2082	0.07	7.94×10^{-17}	Pale discolouration
WI-F-116_1	1895	0.46	2.51×10^{-13}	Orange discolouration

WI-F-116_2	1711	0.49	2.78×10^{-13}	Orange discolouration
WI-F-116_3	2140	0.39	1.77×10^{-14}	Orange discolouration

1576

1577 **Table A5**. Summary of the laboratory data for the 99 lithified ash tuff samples.
1578 Permeability (nitrogen) was measured under a confining pressure of 1 MPa unless
1579 otherwise stated. Photographs of the samples are provided in Figures A8-A11.

1580

Sample	Dry bulk density (kg/m^3)	Connected porosity	Permeability (m^2)	Notes
WI-F-2_1	1366	0.45	2.18×10^{-16}	Alunite
WI-F-2_2	1387	0.44	1.70×10^{-16}	Alunite
WI-F-3_1	964	0.58	1.00×10^{-16}	Alunite; small pores
WI-F-3_2	980	0.57	6.53×10^{-17}	Alunite; small pores
WI-F-4_1	1340	0.42	1.94×10^{-15}	Thin (2-3 mm) low-porosity layer
WI-F-4_2	1306	0.45	4.62×10^{-16}	Thin (2-3 mm) low-porosity layer
WI-F-4_3	1325	0.44	7.88×10^{-18}	Thin (2-3 mm) low-porosity layer
WI-F-4_4	1335	0.43	8.89×10^{-17}	Thin (2-3 mm) low-porosity layer
WI-F-13_1	1134	0.51	4.96×10^{-16}	Alunite
WI-F-13_2	1164	0.49	1.52×10^{-16}	Alunite
WI-F-14	1115	0.51	2.82×10^{-15}	Alunite
WI-F-18	1299	0.45	8.03×10^{-14}	Alunite
WI-F-20_1	1125	0.51	1.22×10^{-13}	
WI-F-20_2	1117	0.52	1.28×10^{-13}	
WI-F-20_3	1147	0.51	1.36×10^{-13}	
WI-F-25_1	898	0.61	3.81×10^{-13}	
WI-F-25_2	943	0.61	3.18×10^{-13}	
WI-F-25_3	922	0.61	2.32×10^{-13}	
WI-F-27_1	1290	0.46	1.55×10^{-15}	Alunite
WI-F-27_2	1347	0.43	1.38×10^{-15}	Alunite
WI-F-27_3	1391	0.42	4.82×10^{-15}	Alunite
WI-F-34_1	1098	0.53	3.01×10^{-13}	
WI-F-34_2	1124	0.51	3.52×10^{-14}	
WI-F-34_3	1134	0.52	4.44×10^{-13}	
WI-F-35_1	1216	0.48	9.97×10^{-14}	
WI-F-35_2	1189	0.49	3.76×10^{-14}	
WI-F-37_1	1393	0.40	2.00×10^{-14}	
WI-F-37_2	1379	0.64	1.08×10^{-14}	
WI-F-42_1	1190	0.50	7.32×10^{-16}	
WI-F-42_2	1200	0.49	6.26×10^{-14}	
WI-F-44_1	911	0.59	4.74×10^{-13}	Alunite
WI-F-44_2	905	0.59	5.19×10^{-13}	Alunite
WI-F-44_3	1059	0.54	2.59×10^{-13}	Alunite
WI-F-46_1	803	0.66	2.73×10^{-13}	Alunite
WI-F-46_2	825	0.65	3.87×10^{-13}	Alunite

WI-F-48	1001	0.57	5.77×10^{-13}	
WI-F-52_1	1493	0.40	2.40×10^{-16}	Alunite; small pores
WI-F-52_2	1506	0.38	8.02×10^{-16}	Alunite; small pores
WI-F-52_3	1498	0.39	9.40×10^{-16}	Alunite; small pores
WI-F-54_1	1553	0.34	2.02×10^{-15}	Alunite; small pores
WI-F-54_2	1474	0.38	5.85×10^{-15}	Alunite; small pores
WI-F-55_1	1269	0.46	9.42×10^{-13}	
WI-F-55_2	1242	0.47	1.26×10^{-12}	
WI-F-56_1	1107	0.49	1.48×10^{-13}	
WI-F-56_2	1122	0.49	2.07×10^{-13}	
WI-F-56_3	1102	0.50	9.66×10^{-14}	
WI-F-59	827	0.67	1.12×10^{-13}	Alunite
WI-F-60_1	1236	0.47	2.40×10^{-14}	Alunite
WI-F-60_2	1191	0.47	2.95×10^{-15}	Alunite
WI-F-63_1	1202	0.50	4.51×10^{-15}	Alunite
WI-F-63_2	1225	0.50	5.03×10^{-15}	Alunite
WI-F-65	1206	0.50	1.29×10^{-12}	
WI-F-66	1192	0.48	3.00×10^{-13}	
WI-F-67_1	1108	0.55	4.98×10^{-13}	
WI-F-67_2	1086	0.55	6.55×10^{-13}	
WI-F-67_3	1086	0.55	7.09×10^{-13}	
WI-F-68_1	1078	0.54	3.54×10^{-14}	Alunite
WI-F-68_2	1076	0.54	Broke	Alunite
WI-F-70_1	1215	0.50	1.51×10^{-12}	
WI-F-70_2	1225	0.50	6.26×10^{-13}	
WI-F-70_3	1201	0.51	1.11×10^{-12}	
WI-F-73	1264	0.49	3.60×10^{-14}	Alunite
WI-F-74	967	0.60	1.51×10^{-12}	
WI-F-75	1498	0.36	1.18×10^{-15}	
WI-F-76	1074	0.52	1.90×10^{-14}	
WI-F-78_1	1264	0.49	3.61×10^{-15}	Alunite
WI-F-78_2	1175	0.52	4.09×10^{-15}	Alunite
WI-F-79_1	1067	0.56	2.66×10^{-13}	Alunite
WI-F-79_2	988	0.57	3.24×10^{-13}	Alunite
WI-F-95_1	1559	0.38	7.38×10^{-14}	
WI-F-95_2	1269	0.50	3.27×10^{-13}	
WI-F-110_1	1521	0.41	8.62×10^{-18}	Alunite; small pores
WI-F-110_2	1474	0.44	2.85×10^{-16}	Alunite; small pores
WI-F-110_3	1531	0.42	6.82×10^{-17}	Alunite; small pores
WI-F-112_1	1486	0.42	2.38×10^{-16}	Alunite; small pores
WI-F-112_2	1505	0.42	4.68×10^{-16}	Alunite; small pores
WI-F-112_3	1445	0.44	4.30×10^{-16}	Alunite; small pores
WI-F-115_1	1133	0.55	4.33×10^{-15}	

WI-F-115_2	1145	0.55	1.40×10^{-16}	
WI-F-118_1	1048	0.56	1.82×10^{-13}	
WI-F-118_2	994	0.55	2.21×10^{-13}	
WI21b_A	1546	0.37	3.09×10^{-15}	Alunite; Elutriation pipes parallel; Pc = 2 MPa
WI21b_C	1410	0.44	1.80×10^{-16}	Alunite; Elutriation pipes parallel
WI21b_D	1511	0.38	6.27×10^{-16}	Alunite; Elutriation pipes parallel
WI21b_E	1412	0.44	1.27×10^{-16}	Alunite; Elutriation pipes parallel
WI21b_H	1363	0.46	1.30×10^{-16}	Alunite; Elutriation pipes perpendicular
WI21b_I	1462	0.42	7.27×10^{-16}	Alunite; Elutriation pipes perpendicular; Pc = 2 MPa
WI21b_J	1195	0.52	1.09×10^{-16}	Alunite; Elutriation pipes perpendicular
WI21_K	1639	0.30	1.47×10^{-16}	Alunite
WI21_20	1282	0.50	1.26×10^{-16}	Alunite
WI22_A	1125	0.52	3.14×10^{-15}	Pc = 2 MPa
WI22_B	1148	0.51	2.29×10^{-15}	
WI22_17	1078	0.50	6.71×10^{-14}	Diameter = 25 mm
WI22_18	1178	0.49	1.55×10^{-13}	Diameter = 25 mm
WI22_22	1163	0.48	1.50×10^{-16}	
WI23_A	1311	0.48	1.21×10^{-15}	Alunite; Pc = 2 MPa
WI23_B	1343	0.45	1.22×10^{-16}	Alunite
WI24_A	1144	0.52	3.08×10^{-13}	Pc = 2 MPa
WI24_B	1144	0.52	2.03×10^{-14}	

1581

1582

1583 **Table A6**. Summary of the laboratory data for the surficial samples (13 jarosite and
1584 sulphur crusts, and 4 ash tuff samples). All values of permeability (nitrogen) were
1585 measured under a confining pressure of 1 MPa. Photographs of the samples are
1586 provided in Figure A12.
1587

Sample	Bulk density (kg/m^3)	Connected porosity	Permeability (m^2)	Notes
WI25_A	2017	0.31	2.63×10^{-12}	
WI25_B	2104	0.32	3.47×10^{-12}	
WI25_C	2128	0.32	2.34×10^{-12}	
WI25_D	2133	0.30	1.89×10^{-12}	
WI25_E	2074	0.31	3.84×10^{-12}	
WI25_F	2041	0.32	5.12×10^{-12}	
WI25_G	2171	0.32	3.04×10^{-12}	
WI25_H	2079	0.32	5.92×10^{-12}	
WI25_I	1915	0.37	6.05×10^{-12}	
WI26_A	1194	0.49	1.11×10^{-12}	
WI26_B	1474	0.40	3.99×10^{-13}	Very high sulphur content
WI26_C	1429	0.46	1.75×10^{-12}	High sulphur content
WI26_D	1314	0.37	7.81×10^{-13}	
WI29_1	1986	0.01	$< 10^{-18}$	Permeability too low for benchtop measurement
WI29_2	1984	0.01	$< 10^{-18}$	Permeability too low for benchtop measurement
WI29_3	1990	0.01	$< 10^{-18}$	Permeability too low for benchtop measurement
WI29_4	1977	0.02	$< 10^{-18}$	Permeability too low for benchtop measurement

1588
1589

1590 **Table A7**. Summary of the laboratory permeability data for the two samples (one lava
1591 sample WI20 and one ash tuff sample WI21b) measured under different confining
1592 pressures (from 1 to 30 MPa). The porosity was 0.05 and 0.37 for the samples WI20 and
1593 WI21b, respectively.
1594

Sample	Confining pressure (MPa)	Permeability (m^2)
WI20	1	1.03×10^{-16}
WI20	2	7.63×10^{-17}
WI20	5	6.63×10^{-17}
WI20	10	5.32×10^{-17}
WI20	15	4.36×10^{-17}
WI20	20	3.62×10^{-17}
WI20	25	3.00×10^{-17}
WI20	30	2.39×10^{-17}
WI21b	1	7.64×10^{-15}
WI21b	2	6.08×10^{-15}
WI21b	5	5.55×10^{-15}
WI21b	10	5.21×10^{-15}
WI21b	15	5.05×10^{-15}
WI21b	20	4.94×10^{-15}
WI21b	25	4.76×10^{-15}
WI21b	30	4.73×10^{-15}

1595